

Utah State University

DigitalCommons@USU

---

All Graduate Theses and Dissertations

Graduate Studies

---

8-2013

## Digital Microfluidics As A Reconfiguration Mechanism For Antennas

Yasin Damgaci  
*Utah State University*

Follow this and additional works at: <https://digitalcommons.usu.edu/etd>



Part of the [Electrical and Electronics Commons](#)

---

### Recommended Citation

Damgaci, Yasin, "Digital Microfluidics As A Reconfiguration Mechanism For Antennas" (2013). *All Graduate Theses and Dissertations*. 1761.  
<https://digitalcommons.usu.edu/etd/1761>

This Dissertation is brought to you for free and open access by the Graduate Studies at DigitalCommons@USU. It has been accepted for inclusion in All Graduate Theses and Dissertations by an authorized administrator of DigitalCommons@USU. For more information, please contact [digitalcommons@usu.edu](mailto:digitalcommons@usu.edu).



DIGITAL MICROFLUIDICS AS A RECONFIGURATION MECHANISM FOR  
ANTENNAS

by

Yasin Damgaci

A dissertation submitted in partial fulfillment  
of the requirements for the degree

of

DOCTOR OF PHILOSOPHY

in

Electrical Engineering

Approved:

---

Dr. Bedri A. Cetiner  
Major Professor

---

Dr. Jacob Gunther  
Committee Member

---

Dr. Reyhan Baktur  
Committee Member

---

Dr. Edmund Spencer  
Committee Member

---

Dr. T.C. Shen  
Committee Member

---

Dr. Mark R. McLellan  
Vice President for Research and  
Dean of the School of Graduate Studies

UTAH STATE UNIVERSITY  
Logan, Utah

2013

Copyright © Yasin Damgaci 2013

All Rights Reserved

# Abstract

Digital Microfluidics as a Reconfiguration Mechanism for Antennas

by

Yasin Damgaci, Doctor of Philosophy

Utah State University, 2013

Major Professor: Dr. Bedri A. Cetiner  
Department: Electrical and Computer Engineering

This dissertation work concentrates on novel reconfiguration technologies, including design, microfabrication, and characterization aspects with an emphasis on their applications to multifunctional reconfigurable antennas. In the literature, reconfigurable antennas have made use of various reconfiguration techniques. The most common techniques utilized revolved around switching mechanisms. Other techniques such as the incorporation of variable capacitors, varactors, and physical structure manipulation surfaced recently to overcome many problems faced in using switches and their biasing. Usage of fluids (microfluidic or otherwise) in antennas provides a conceptually easy reconfiguration mechanism in the aspect of physical alteration. However, a requirement of pumps, valves, etc. for liquid transportation makes the antenna implementations rather impractical for the real-life scenarios. This work reports on design and experiments conducted to evaluate the electrowetting on dielectric (EWOD) driven digital microfluidics as a reconfiguration mechanism for antennas. There are three approaches developed for the designing of this new type reconfigurable digital-microfluidic antenna. The first approach is based on the unique metamaterial transmission line structures, which are leading to antenna miniaturization. Coplanar waveguide (CPW) metamaterial transmission lines (TLs) were designed and used as digital microfluidic platforms, where tunable resonance frequency was demonstrated for radio frequency

(RF)/microwave applications. The maximum tuning range achieved was around 400 MHz (from 3.51 GHz to 3.92 GHz) with a DC actuation voltage of 110 V. The second methodology was based on annular slot antenna integration with a microfluidic chip, which consists of EWOD platform having mercury droplet within it. This droplet was spread out by electrostatic actuation, thereby resulting in reversible reconfigurable impedance properties. This reconfigurable antenna was designed, fabricated, and measured. The frequency of operation is tuned from 11.4 GHz to 13 GHz as demonstrated by simulations and measurements from the fabricated prototype. The third methodology was proposing a tunable component using superhydrophobic micro-structured surfaces. These surfaces, along with tunable wetting techniques, can be used for transition from the superhydrophobic Cassie state to the normal Wenzel wetting state to build a variable capacitive device (analog varactor, a switched capacitor) or a low-loss switch. Fabrication and measurement results were presented for a low voltage capacitive switch, which could be an alternative to the micro-electromechanical systems (MEMS) counterparts.

## Public Abstract

Digital Microfluidics as a Reconfiguration Mechanism for Antennas

by

Yasin Damgaci, Doctor of Philosophy

Utah State University, 2013

Major Professor: Dr. Bedri A. Cetiner  
Department: Electrical and Computer Engineering

The properties of conventional antennas are fixed by the initial design and cannot be changed. A reconfigurable antenna, on the other hand, can dynamically change its properties, and it can adjust its behavior for a given propagation condition. This dissertation work concentrates on novel reconfiguration technologies, including design, microfabrication, and characterization aspects with an emphasis on their applications to multifunctional reconfigurable antennas. In the literature, reconfigurable antennas have made use of various reconfiguration techniques. The most common techniques utilized revolved around switching mechanisms. Other techniques such as the incorporation of variable capacitors, varactors, and physical structure manipulation surfaced recently to overcome many problems faced in using switches and their biasing. Usage of fluids (microfluidic or otherwise) in antennas provides a conceptually easy reconfiguration mechanism in the aspect of physical alteration. However, a requirement of pumps, valves, etc. for liquid transportation makes the antenna implementations rather impractical for the real-life scenarios. This work reports on experiments conducted to evaluate the electrowetting on dielectric (EWOD) driven digital microfluidics as a reconfiguration mechanism for antennas. EWOD is direct manipulation technique of liquids with electrostatic actuation. There are three approaches developed for the designing these new type antennas. The first approach is based on the

unique metamaterial transmission line structures which are leading to antenna miniaturization. The following methodology is based on antenna integration with a microfluidic chip which consists of an EWOD platform having a mercury droplet within it. The third methodology proposes a tunable component using superhydrophobic micro-structured surfaces. These surfaces, along with tunable wetting techniques, can be used for transition from the superhydrophobic Cassie state to the normal Wenzel wetting state to build a variable capacitive device (analog varactor, a switched capacitor) or a low-loss switch. Results are demonstrated by simulations and measurements from the fabricated prototypes.

## Acknowledgments

This work was only possible due to the guidance and support of many people.

I would like to use this place to acknowledge the support given by Dr. Bedri Cetiner, Dr. Mehmet Unlu, and Dr. Necmi Biyikli. They taught me many things about antennas, microwaves, micro-mechanical systems, and microfabrication. Furthermore, I would like to thank my committee members for their insight, valuable suggestions, and time.

Working with my fellow students at Utah State University, Bilkent University (Engin Cagatay, Mehmet Alican Noyan), and Universitat Politecnica de Catalunya (Daniel Rodrigo Lopez, Jordi Balcells, Maria Alonso) has been both enriching and enjoyable. I am grateful to have such good friends and colleagues.

The Cornell Nanoscale Facility staff has all been very helpful and a pleasure to work with.

Thank you also to my family for all their support over these years.

Yasin Damgaci



# Contents

	Page
<b>Abstract</b> . . . . .	<b>iii</b>
<b>Public Abstract</b> . . . . .	<b>v</b>
<b>Acknowledgments</b> . . . . .	<b>vii</b>
<b>List of Figures</b> . . . . .	<b>x</b>
<b>1 Introduction</b> . . . . .	<b>1</b>
1.1 Reconfigurable Antennas . . . . .	1
1.2 Reconfiguration Mechanism . . . . .	2
1.3 Contributions of This Dissertation . . . . .	3
1.4 Dissertation Outline . . . . .	4
<b>2 Literature Review</b> . . . . .	<b>5</b>
2.1 Reconfiguration Mechanisms . . . . .	5
2.1.1 Discrete Electronic Components . . . . .	5
2.1.2 Tunable Materials . . . . .	10
2.1.3 Mechanical/Structural Changes . . . . .	13
2.2 Fluidic Antennas . . . . .	15
<b>3 Digital Microfluidics</b> . . . . .	<b>18</b>
3.1 Continuous-Flow Microfluidics . . . . .	18
3.2 Digital (Droplet-Based) Microfluidics . . . . .	19
3.3 Electrowetting Theory . . . . .	19
3.3.1 Electromechanical Model of EWOD . . . . .	22
3.3.2 Limitations of EWOD . . . . .	27
<b>4 Tunable Zeroth-Order Resonator Antenna Based on EWOD</b> . . . . .	<b>29</b>
4.1 Metamaterials . . . . .	29
4.2 Zeroth-Order Resonator . . . . .	32
4.3 Tunable Zeroth-Order Resonator Transmission Line . . . . .	34
4.3.1 Design . . . . .	34
4.3.2 Fabrication . . . . .	36
4.3.3 Experimental Results . . . . .	37
4.4 Antenna Application . . . . .	39
<b>5 A Frequency Reconfigurable Antenna Based on EWOD</b> . . . . .	<b>42</b>
5.1 Design and Working Mechanism . . . . .	42
5.2 Fabrication . . . . .	46
5.3 MRA Prototype Characterization . . . . .	47

<b>6 RF Switch Based on Reversible Wetting States on Superhydrophobic Sur-</b>	
<b>faces . . . . .</b>	<b>52</b>
6.1 Superhydrophobic Surfaces . . . . .	52
6.2 Switching of Wetting States on Superhydrophobic Surfaces . . . . .	55
6.3 RF Switch . . . . .	57
<b>7 Conclusions and Future Work . . . . .</b>	<b>62</b>
<b>References . . . . .</b>	<b>64</b>
<b>Appendix . . . . .</b>	<b>71</b>
<b>Vita . . . . .</b>	<b>74</b>

## List of Figures

Figure	Page
2.1 Different configurations for the antenna structure. . . . .	6
2.2 Reconfigurable pixel-patch antenna and radiation diagrams for pattern re-configuration. . . . .	8
2.3 The reconfigurable fractal antenna structure. . . . .	8
2.4 Multi-part antenna with switches used to extend the spiral microstrip line length and achieve a circular polarization. . . . .	9
2.5 Reconfigurable antenna geometries (a) Planar version (b) Volumetric version.	11
2.6 Antenna where the patch was bent to achieve reconfiguration. . . . .	13
2.7 Mechanically reconfigurable impedance surface consisting of two printed circuit boards: a high-impedance ground plane and a separate tuning layer. The tuning layer is moved across the stationary high-impedance surface to vary the capacitance between the overlapping plated and tune the resonance frequency of the surface. . . . .	14
2.8 A horizontally polarized antenna couples energy into leaky modes on the tunable impedance surface. The waves propagate across the surface and radiate at an angle governed by the surface resonance frequency with respect to the excitation frequency. By tuning the surface resonance frequency, the beam is steered in the elevation plane. . . . .	15
2.9 Fabricated test antenna with capillaries. . . . .	16
2.10 Diagram of the coaxially fed DRA using colloidal dispersions. . . . .	16
2.11 Stretchable antenna. . . . .	17
3.1 The electrowetting effect in an air ambient. The left image illustrates the initial contact angle with no voltage applied, and the right image illustrates the new contact angle once a bias is introduced. . . . .	21
3.2 Droplet on an ideal hydrophobic surface. In the left image, no potential is applied. In the right, a potential is applied between the substrate and polar liquid. . . . .	21

3.3	Common electrowetting architectures (a) Open system (b) Covered system.	22
3.4	Schematic of the electric charge distribution in the vicinity of the triple contact line. Electric charges are located at the solidliquid interface and at the liquidgas interface, approximately within a distance $d$ from the solid surface. In reality, this is a very simplified view since the liquid interface is distorted by the electric forces very close to the triple contact line. . . . .	25
4.1	Equivalent circuit models. (a) Homogeneous RH TL (b) Homogeneous LH TL (c) Homogeneous CRLH TL. . . . .	30
4.2	Dispersion diagrams corresponding to the TLs. . . . .	33
4.3	Resonance modes corresponding to the TLs. . . . .	33
4.4	Equivalent circuit of a capacitor loaded CPW. . . . .	35
4.5	The layout and test schematic of the tunable CPW metamaterial TL. $p = 2, w = 1.395, s = g = 0.07, r_1 = 0.75, r_2 = 0.7, r_3 = 0.1, r_4 = 0.05$ (units in mm). . . . .	37
4.6	Cross section (A-A') view of the structure and EWOD principle. . . . .	37
4.7	The photographs of a fabricated device (a) before and (b) after mercury droplet dispensing. The boundaries of the base contact areas are illustrated with white and red dash lines before and after EWOD spreading, respectively, $(r_2 - r_2 \ 150\mu m)$ . . . . .	38
4.8	Simulated and measured (a) S11 (b) S21 parameters before and after applied voltage of 110 Volts (c) Calculated propagation constant of the unit cell structure. . . . .	40
4.9	ADS and HFSS models of the proposed antenna and reflection coefficient after matching. . . . .	41
5.1	(a) 3-D schematic of the MRA integrated with a microfluidic chip. The inset shows the magnified view of the microfluidic chip; (b) Top view of the MRA with magnified views of the CPW feed and EWOD platform (1 and 2 are the radii of the contact base area of Mercury droplet, before and after spreading). The design dimensions are: $r_1 = 4.1, r_2 = 3.9, r_c = 1.3, r_3 = 0.1, r_4 = 0.5, w_1 = 1, w_2 = 0.1, w_3 = 0.05, g_1 = 0.015, g_2 = 0.0115, g_3 = 0.025, l_1 = 4.5, l_2 = 0.45, l_3 = 0.7, d_1 = d_2 = 0.2, h_1 = 1, h_2 = 1, 1 \cong 0.320, 2 \cong 0.470$ (units in mm). . . . .	45
5.2	The process flow for fabricating the frequency reconfigurable antenna integrated with a microfluidic chip. . . . .	47

5.3	The photographs of (a) the top view of a fabricated MRA prototype; and (b) an empty, mercury filled, and mercury + silicone oil filled microfluidic chips.	50
5.4	Measured and simulated reflection coefficients and radiation patterns corresponding to $f=11$ GHz (ON state) and $f=13$ GHz (OFF state) modes of operations.	51
6.1	SEM image of a Lotus leaf.	53
6.2	Superhydrophobic surfaces (a) Cassie-Baxter (b) Wenzel states.	54
6.3	Schematic of capacitive RF switch.	58
6.4	Circuit model of capacitive RF switch.	59
6.5	Fabricated RF switch.	60
6.6	Measurement set-up and results.	61
A.1	Cross section view of a micro-drop dispensed on a hydrophobic surface.	73
A.2	Schematic of a droplet for volume integration.	73

# Chapter 1

## Introduction

Modern wireless Radio-Frequency (RF)/microwave systems have experienced an explosive growth within recent years. Increasing demands on capacity, higher data rates, multi-mission functionality introduces a requirement to perform a multitude of functions across several frequency bands and operating bandwidths. In most cases, these requirements cannot be served by a single antenna but rather require the use of multiple antennas of varying form-factors and geometries. Antenna is the interface between the transceiver and the free space. Reconfigurable antennas can deliver the same throughput as a multi-antenna system using dynamically variable and adaptable single-antenna geometry without increasing the physical number required to accommodate these antennas. Reconfigurable antennas can thus provide great versatility in applications such as cognitive radio, multiple-input and multiple-output (MIMO) systems, Radio-Frequency Identification (RFID), smart antennas, etc.

### 1.1 Reconfigurable Antennas

Reconfigurable antennas have existed for many years and have many examples. Reconfiguration of an antenna is achieved through an intentional redistribution of the currents or, equivalently, the electromagnetic fields of the antennas effective aperture, resulting in reversible changes in the antenna impedance and/or radiation properties. These changes are enabled through various mechanisms such as switching, material tuning, and structural modifications. Thus, under this definition, the traditional phasing of signals between elements in an array to achieve beam forming and beam steering does not make the antenna reconfigurable because the antennas basic operating characteristics remain unchanged in this case [1,2].

## 1.2 Reconfiguration Mechanism

The choice of reconfiguration mechanism presents trade-offs in functionality and complexity as well as device or system lifetime. For instance, mechanisms that rely on movable parts to facilitate reconfiguration (e.g., RF micro electro mechanical systems (RF MEMS)) may experience mechanical wear or failure from hot-switching. However, they are typically actuated electrostatically and the performance they provide over solid-state designs low intrinsic losses and power consumption (especially at higher frequencies) often offsets the potential for a degraded lifetime and failure of the device. As another example, the integration of tunable materials for the antenna design can cause an entirely different set of problems if the material properties or tunability degrades over time. Both degradations in the performance are in addition to the complexity and integration of the antenna, reconfiguration mechanism, and supporting structures (bias, control, etc.). Therefore, selection of the reconfiguration mechanism should be made carefully, with system lifetime, cost, complexity, and desired performance levels and losses considered from the outset [3].

Although reconfigurable antennas come in a large variety of different shapes and forms [4], it is possible to group them into four main categories based on their reconfigurability function as:

- A frequency reconfigurable antenna,
- A radiation pattern reconfigurable antenna,
- A polarization reconfigurable antenna,
- Combinations of the above stated categories (Multifunction Reconfigurable Antenna MRA).

In the case of frequency reconfigurable antennas, frequency tuning occurs for different antenna configurations. This frequency tuning manifests itself in resonance shifting in a return loss data. In the case of reconfigurable radiation pattern antennas, radiation patterns change in terms of shape, direction, or gain. In the case of a reconfigurable polarization antenna, polarization types change for every antenna configuration. In the last category,

antennas exhibit many properties combined together to yield, for example, a reconfigurable return loss with reconfigurable polarization. Reconfigurable antennas can also be further classified into three main groups based on their reconfiguration mechanisms:

1. Antennas using discrete electronic components,
2. Antennas using tunable materials,
3. Antennas using physical/mechanical alteration.

The most common technique for reconfiguration is switching. For switching, either Microelectromechanical System (MEMS) or solid-state switching devices can be employed. MEMS have been the preferred technology due to the monolithic integration capability with antenna segments along with their low loss and power characteristics. Also, the potential of MEMS in avoiding nonlinearity and intermodulation effects is an important advantage over solid-state switching devices. However, the long-term reliability of MEMS and complex packaging processes along with associated high-cost still remain to be the main bottlenecks for MEMS integrated reconfigurable antennas.

### **1.3 Contributions of This Dissertation**

In this dissertation, a novel reconfiguration technique based on digital microfluidics was employed. This technique can be included in the physical/mechanical alteration group, but it is much more simple and at a lower cost compared to previous MEMS-based techniques. By using liquid metal droplets, antenna itself was created and deformation and manipulation were carried out on the antenna element itself without using any complex circuitry or different circuit components. As a result, the ability to manipulate the liquids changes the geometry of the antenna, which in turn changes the current distribution resulting into the desired reconfigurable mode of operation. In summary, with this new reconfiguration mechanism, it is possible to achieve a lower complexity and cost as compared to prior art of reconfiguration mechanisms.



#### **1.4 Dissertation Outline**

The outline of the dissertation is organized as follows: Chapter 2 describes the details of reconfiguration mechanisms and fluidics antennas; Chapter 3 focuses on the theoretical background of digital microfluidics; Chapter 4 presents the simulated and measured results for reconfigurable metamaterial transmission lines; Chapter 5 demonstrates the design, fabrication, and test work on the X band frequency reconfigurable antenna; Chapter 6 deals with a novel RF switch design based on superhydrophobic surfaces; and eventually, the dissertation is concluded in Chapter 7, where the future work plan is also included.

## Chapter 2

### Literature Review

#### 2.1 Reconfiguration Mechanisms

The reconfiguration of an antenna may be achieved through many techniques. Some designers resort to circuit elements while others rely on mechanical alteration of the structure such as rotating or bending of one or more of its parts [5]. Yet another approach is biasing different antenna parts at different times, reconfigure the feeding networks, or appropriately excite the antenna arrays. All such approaches have significantly contributed to the evolution of reconfigurable antennas during the last decade. More recently, antenna designers have used electrically-actuated switches and variable capacitors in order to achieve reconfiguration [6]. p-i-n (PIN) diodes and RF-MEMS are some of the most widely used electrically actuated devices [7–23].

##### 2.1.1 Discrete Electronic Components

The effective length the antenna, and hence its operating frequency, can be changed by adding or removing part of the antenna length through electronic, optical, mechanical, or other means. Groups have demonstrated different kinds of switching technology, such as optical switches, PIN diodes, Field-Effect Transistors (FETs), and RF-MEMS switches [24–30].

In general form, the antenna with switches, shown in Fig. 2.1 [31], is composed of different patches connected together by switches. The conceptual antenna provides ten different reconfigurable modes of operation corresponding to the combination of two operating frequencies (4.1 and 6.5 GHz) and five reconfigurable polarizations of the radiated field (linear X, linear Y, dual linear, right hand circular, and left hand circular).

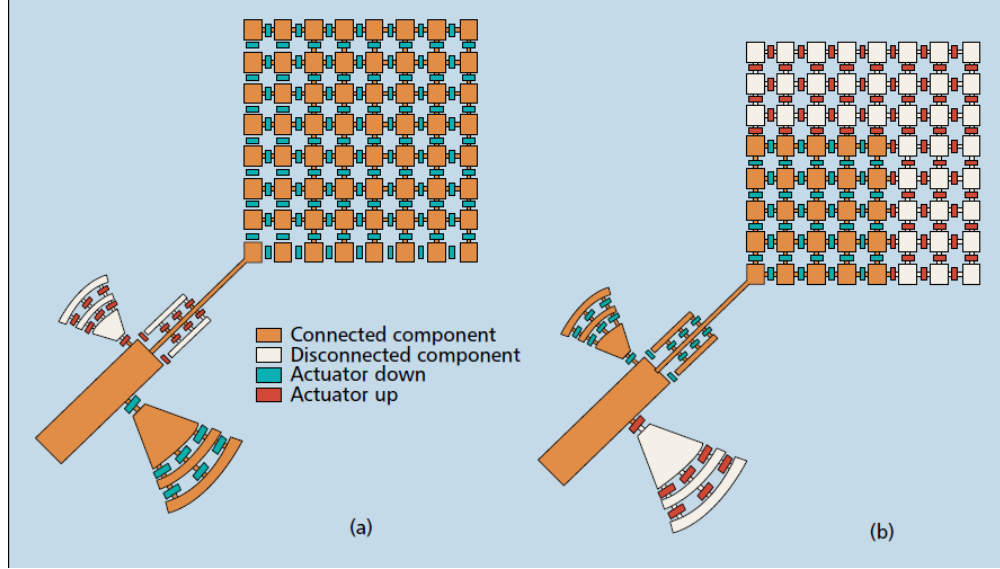


Fig. 2.1: Different configurations for the antenna structure.

Micro-electromechanical systems (MEMS) RF switches make use of micro-machined beams or membranes that are deflected to open or close an RF circuit in either a series or shunt configuration. The micro-machined beams can be designed for either direct (ohmic) or capacitive-coupled contact with the RF circuit. The beams are typically attached at one end (cantilever) or attached at both ends (fixed-fixed beam or membrane). Actuation of the beams can be accomplished using various techniques, including electrostatic, electromagnetic, piezoelectric, or thermo-mechanical. Electrostatic actuation is most commonly used due to the relative ease of generating electric fields at the microscopic level, fast response times, and low-power consumption [32]. RF MEMS switches have several attractive features over PIN diodes or other solid-state switches, including lower insertion loss, higher isolation, low dc power consumption, and relatively high power handling. However, the MEMS switches do have certain disadvantages, including the requirement for high activation voltages, higher cost, lower reliability, and limited commercial availability. For ohmic-contact switches, one of the main sources limiting reliability is the increased resistance, which eventually occurs due to damage, pitting, and hardening of the contact area due to the impact force between the beam and the contact. Micro-welding can also be a

serious problem for switches handling higher RF power (100 mW to 1000 mW), where the power dissipated in the ohmic resistance enough to cause the beam to weld to the contact, resulting in a failure for the switch to open. For capacitive switches, the main source of failure is due to stiction (the inability of the switch to release once the pull-down voltage is removed) between the dielectric layer and the metal layer. This results from the relatively large contact area, where the charging effects of the dielectric layer either cause the switch to stick in the downstate position, or results in an increase in the pull-down voltage, making the switch unusable. Furthermore, due to the MEMS sensitivity to moisture and dirt, the device needs to be hermetically sealed in a nitrogen environment, which increases the cost of these devices.

Electrostatic actuators (voltage driven) have very low-power consumption ( $\mu W$  range) compared to the  $mW$  range for electromagnets, but require higher activation voltages (typically 20 V to 70 V). Piezoelectric actuators rely on the deformation of structures caused by the motion of internal charges as a result of an applied electric field [33]. They typically make use of exotic materials, such as lead-zirconate-titanate (PZT), but may require somewhat lower activation voltages. Electromagnetic actuators are current driven and thus require lower actuation voltages, but they consume higher dc power, and it is difficult to realize the required multi-turn magnetic windings on a small scale. MEMS switches have been integrated with various antennas, including microstrip patches, and slots, for the design of reconfigurable antennas.

A pixelized structure [27] is shown in Fig. 2.2. The proposed reconfigurable pixel-patch antenna architecture is built on a number of printed rectangular shaped metallic pixels interconnected by RF MEMS actuators on a quartz substrate.

The fractal structure [8], shown in Fig. 2.3, is reconfigured using RF MEMS switch. The basic antenna is a  $130^\circ$  balanced bowtie. A portion of the antenna corresponds to a two iteration fractal Sierpinski dipole. The remaining elements are added (three elements on each side) to make the antenna a more generalized reconfigurable structure.

Two designs based on a spirally shaped patch [29,30] use switches to extend or shorten

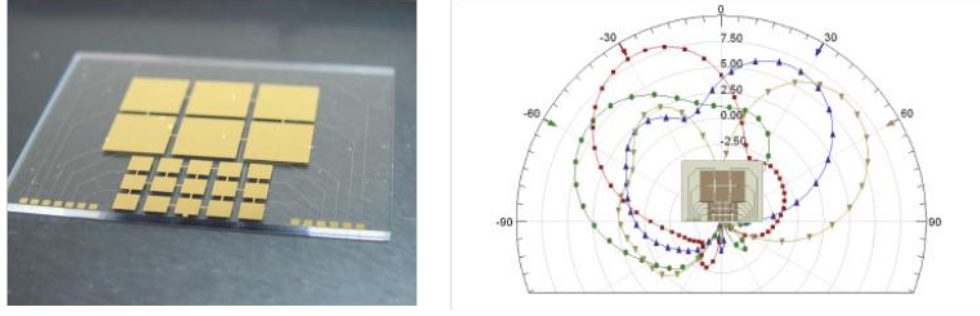


Fig. 2.2: Reconfigurable pixel-patch antenna and radiation diagrams for pattern reconfiguration.

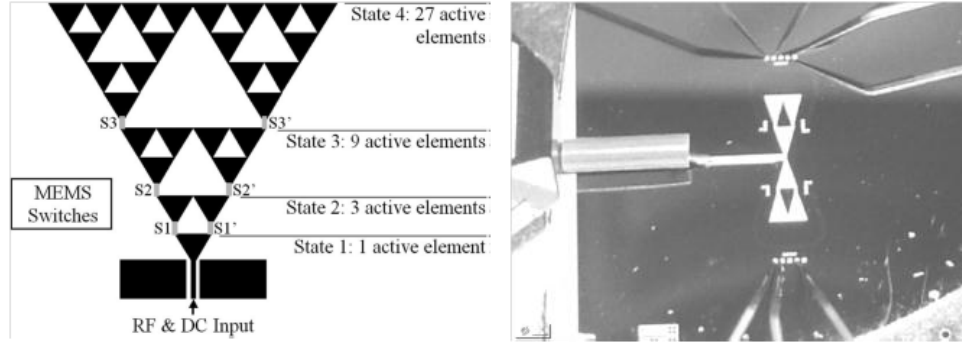


Fig. 2.3: The reconfigurable fractal antenna structure.

the length of a spiral arm. The spiral arm shaped patch antenna [29] is shown in Fig. 2.4. This spiral shaped patch is printed on the dielectric substrate and is fed in the center through a coaxial cable. Using the coaxial feed, the antenna is excited through a vertical probe, which is formed by extending the inner conductor of the coaxial line while the external side of the coax is connected to the ground plane in the back of the substrate. The spiral antenna consists of five sections that are connected with four RF-MEMS switches. The location of switches is determined such that the axial ratio and gain of the antenna are optimum at the frequency of interest. This antenna achieves resonance tuning and reconfigurable polarization.

A PIN diode is a semiconductor device that exhibits nonlinear behavior in terms of its current as a function of voltage (IV) characteristics. The diode can be made to behave as

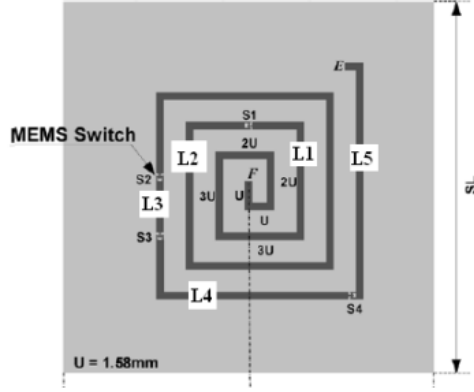


Fig. 2.4: Multi-part antenna with switches used to extend the spiral microstrip line length and achieve a circular polarization.

either a short circuit (ON state) or an open circuit (OFF state), depending on whether the biasing dc voltage across its terminals is positive or negative, respectively. This behavior has been exploited in the design of PIN diodes as RF switches. PIN-diode switches are relatively inexpensive devices, and readily available in a variety of commercial packages of rectangular or cylindrical shape, with maximum dimensions as small as a few millimeters. They offer relatively fast switching times, but since they draw current in the On state, they have a relatively high dc power consumption. Another important parameter is the maximum RF power that the diode switch can support, which is limited by the maximum power dissipation allowable for the diode. The maximum RF signal power that the diode can accommodate will differ depending on whether it is configured as a series or a shunt switch. (Typically, PIN diodes can handle on the order of tens of watts, which will limit their use in high-power applications.) PIN diodes have been integrated into various antennas as switches in order to implement discrete frequency tuning at two or more frequencies. Examples include printed dipoles, slot antennas, microstrip-patch antennas, and dielectric resonator antennas [33].

Field-effect transistors (FETs) can also be used as microwave switches. The FET is a device with three terminals, identified as the source, drain, and gate. The flow of RF current between the source and drain can be turned on or off by adjusting the relative

bias voltage on the gate. The FET switch draws practically no DC current in either the On or Off state, giving it an advantage over the PIN-diode switch in terms of a lower DC power consumption. FET switches have been used in the design of reconfigurable microstrip antennas, slot antennas, and printed dipoles [34].

A varactor, or variable capacitor, is a circuit element, typically based on a p-n junction semiconductor device, the capacitance of which can be controlled by the application of a bias voltage. The variable junction capacitance is controlled by the applied DC voltage across the varactors terminals. Like PIN diodes and FET switches, a wide variety of varactors are readily commercially available. The varactor also draws negligible current, and thus has a low DC power consumption. Varactors have been used with various antennas, including microstrip patches, slots, dipoles, and dielectric resonator antennas, for designing reconfigurable antennas with continuous frequency tuning [35].

An example design reconfigured by variable capacitors [12] is shown in Fig. 2.5. The antenna is a  $2 \times 2$  reconfigurable planar wire grid antenna designed to operate in free space. Variable capacitors are placed in the centers of 11 of the 12 wire segments that comprise the grid. The center of the 12th segment, located on the edge of the grid, is reserved for the antenna feed. An antenna size of 4 cm x 4 cm is assumed for this design. The values of the variable capacitors are constrained to lie between 0.1 pF and 1 pF. These capacitors are then adjusted using a robust Genetic Algorithm (GA) optimization technique in order to achieve the desired performance characteristics for the antenna. This antenna exhibits resonance tuning.

### 2.1.2 Tunable Materials

Tunable materials, which are materials with inherent electrical properties (permittivity, permeability, or conductivity) of which can be controlled by the application of an external bias (electric, magnetic, or optical). Examples of tunable substrates include ferroelectrics, ferrites, liquid crystals, and semiconductors. These materials can be incorporated as an integral part of the antenna, and alteration of their electrical properties translates into a shift in operating parameters.

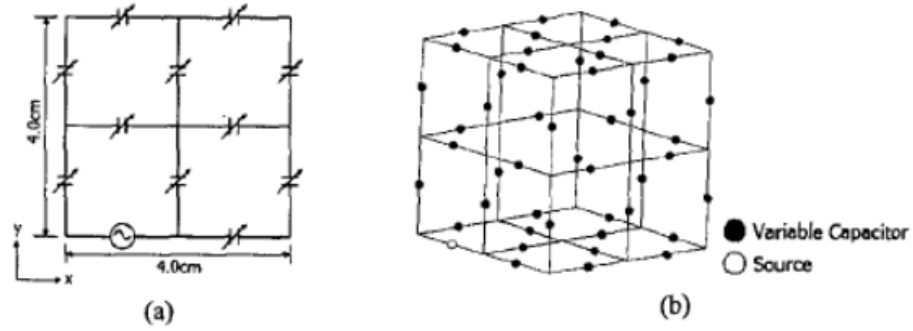


Fig. 2.5: Reconfigurable antenna geometries (a) Planar version (b) Volumetric version.

Ferrites are ceramic-like material made from sintering a mixture of metallic oxides. They are characterized by a relative permeability of several thousand at low frequencies, dielectric constants of 10 or greater, and high values of resistivity. Ferrites have found widespread applications as cores (used in inductors, transformers, and electromagnets), beads (for suppressing high-frequency noise in electronic components), and powders used for magnetic-recording tapes. Commercially available microwave ferrite materials include magnesium, nickel, and lithium ferrites, and various yttrium iron garnets (YIGs). These ferrite materials are available in various shapes, including sheets and rods of circular or rectangular cross section. At microwave frequencies, ferrites are used in such devices as isolators, circulators, and phase shifters. The important property of ferrites that is exploited in the design of reconfigurable antennas at microwave frequencies is the change in permeability with the application of a dc magnetic field. Ferrites currently have the lowest losses and highest tuning ranges among the tunable materials. They can also be readily integrated with printed-antenna technology. Their main drawback is the relatively complex biasing requirements (they require an electromagnet or wire coil, or a movable permanent magnetic) and higher dc power consumption, due to the need for a constant bias current.

Ferroelectric substrates offer a behavior analogous to ferrites, where the permittivity of the ferroelectric can be altered by the application of a static electric field. This behavior is the property of certain classes of crystals exhibiting a spontaneous polarization that can



be reversed by the application of an electric field. Metal oxides known as perovskites, characterized by the common formula  $ABO_3$  (such as titanates,  $BaTiO_3$ , and niobates,  $KNbO_3$ ), have the requisite crystal structure for this behavior [36]. The dielectric constants for these materials are typically on the order of several hundred.

Liquid crystals are fluids that exhibit a phase state with a certain degree of ordering in the arrangement of its molecules, which lies between the crystalline solid state (at low temperatures) and the ordinary liquid state (at high temperatures). Liquid crystals have been used for many years at optical frequencies in displays for numerous types of electronic equipment, and more recently for flat-screen televisions. To date, only a limited amount of research has been carried out to examine the use of liquid crystals at microwave or millimeterwave bands. For microwave applications, the liquid crystals have a behavior similar to that of paraelectrics, where an applied electric field can alter the dielectric constant of the material. In liquid crystals, this change in dielectric constant arises from a change in the orientation of the molecules in response to an applied electric field. The dielectric constants of liquid crystals are much lower than in ferroelectrics, with values typically between 2.5 and 4, making them more amenable to integration with printed antennas. A tunability of up to about 30% has been achieved at microwave frequencies, with bias voltages on the order of 15 V to 20 V, which is much lower than the bias voltages required for paraelectric materials. Power consumption is also relatively low. One of the disadvantages of liquid crystals is that they must be kept between about 20°C to 35°C in order to stay in the liquid-crystal phase.

Rainville and Harackiewicz [37] presented a polarization-tunable microstrip antenna based on static magnetic biasing of a ferrite film. As with microstrip antenna on bulk ferrite substrates [38, 39], the co-polarized fields are much less dominant than those from a traditional microstrip patch antenna. Rainville and Harackiewicz [37] took advantage of the fact that the applied static bias field tuned the frequency of the cross-polarized field to create a range of elliptical polarizations. Optimization of feed point and ferrite film properties could result in purely circular and linear polarizations as well.

### 2.1.3 Mechanical/Structural Changes

Reconfigurability can be achieved in many radiators by deforming the physical shape of an antenna or by altering the antennas dimensions. This approach is best suited for resonant-type antennas, where a change in one or more dimensions will cause a shift in the resonant frequency. This is typically accomplished through the use of a mechanical actuator. Actuators come in a myriad of forms and sizes, and can be designed for various applications ranging from the precision micron control of delicate optical components to the displacement of large masses. Instead of using actuators that are integrated into the antenna to execute the desired change in dimensions, antennas could potentially be made up of inherently deformable material. Examples of such materials include electro-active polymers and shape-memory alloys [40].

The first design that used a mechanical structural change to achieve reconfiguration [40] is shown in Fig. 2.6. The antenna is fabricated over a sacrificial layer residing on the substrate. A thin layer of magnetic material is then electroplated on the antenna surface. By etching away the sacrificial layer between the antenna and substrate, the antenna is released and connected only by its feed line. When an external field is applied, the flexible region created at the junction between the released and unreleased microstrip line is plastically deformed, and the structure is bent by an angle. After this plastic deformation, the antenna remains at a certain rest angle above the substrate even after the field is removed. This antenna exhibits resonance tuning.

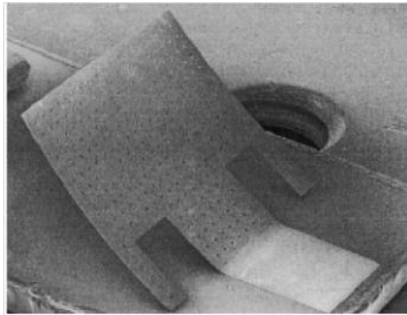


Fig. 2.6: Antenna where the patch was bent to achieve reconfiguration.

With the reflective surface physically removed and isolated from the primary feed, reflector antennas are a natural choice for applications that require radiation pattern reconfigurability independent of frequency. Changes in an effective reflector have been demonstrated using reconfigurable high-impedance surfaces [41]. A lattice of small resonant elements produces high-surface impedance near their resonant frequency, creating, in effect, an artificial ground plane. Changing the capacitances between resonant elements across the lattice through mechanical means creates a phase gradient that can produce a steered beam when the lattice is used as a reflector [42]. A closely related approach has also been used to develop a reconfigurable leaky-wave antenna using mechanical tuning [43]. In this case, a horizontally polarized antenna is used to couple energy into leaky transverse electric waves on a tunable impedance surface. A diagram of the surface, including the moveable top capacitance surface, is shown in Fig. 2.7. The radiated beam from the surface can be steered in elevation over a range of  $45^\circ$  by changing the apparent capacitance of the surface through mechanically shifting the top capacitive plane. The antenna and surface are shown in Fig. 2.8. An electronically tuned version of this antenna that uses varactors can produce reconfigurable backward as well as forward leaky-wave beams [44, 45].

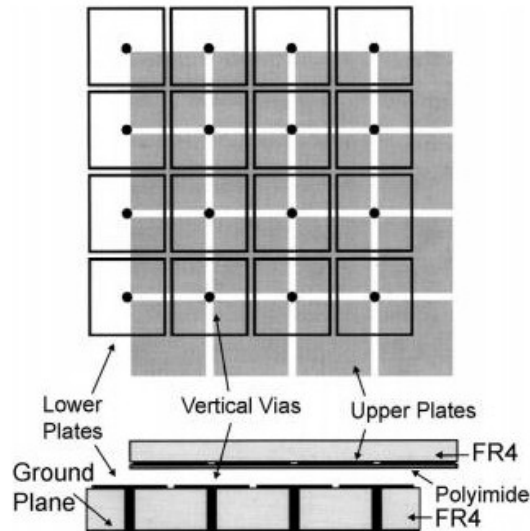


Fig. 2.7: Mechanically reconfigurable impedance surface consisting of two printed circuit boards: a high-impedance ground plane and a separate tuning layer. The tuning layer is moved across the stationary high-impedance surface to vary the capacitance between the overlapping plated and tune the resonance frequency of the surface.

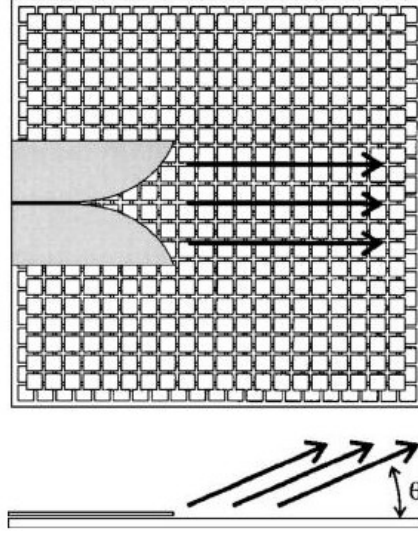


Fig. 2.8: A horizontally polarized antenna couples energy into leaky modes on the tunable impedance surface. The waves propagate across the surface and radiate at an angle governed by the surface resonance frequency with respect to the excitation frequency. By tuning the surface resonance frequency, the beam is steered in the elevation plane.

## 2.2 Fluidic Antennas

Fluidic systems have been proposed for antenna reconfiguration, which can be categorized as a subset for the mechanical/structural changes group. Fluidic conductors have been used in stretchable dipoles [46] and patch antennas [47]. All of these antennas, however, require precise mechanical positioning in order to tune to the correct frequency, which can be difficult and expensive to do. The positioning will also be significantly slower than the methods discussed previously. Alternatively, the reconfiguration mechanism can consist of fluidic dielectrics, which will effectively change the electrical size of a radiating element.

The antenna shown in Fig. 2.9 is a frequency reconfigurable patch antenna enabled by a simple pressure-driven capillary and fluidic colloidal dispersions. Prepared dispersions were injected into capillaries 1 and 3 of this antenna for reconfigurability.

Another fluidic reconfigurable antenna, shown in Fig. 2.10, is a frequency reconfigurable dielectric resonator antenna (DRA) [48]. The coaxial probe-fed structure has tunable impedance properties that are reversibly controlled by adjusting the columnar height of the

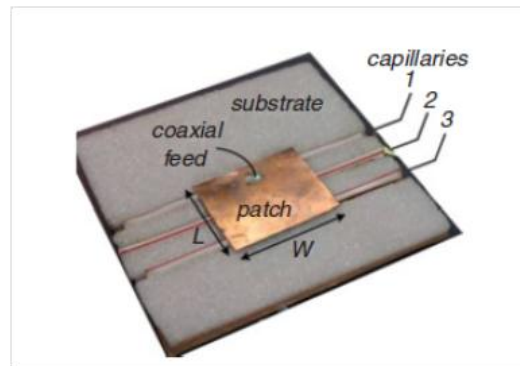


Fig. 2.9: Fabricated test antenna with capillaries.

dispersion. Colloidal barium strontium titanate was dispersed in hydrotreated naphthenic oil and placed at several heights into a section of polycarbonate tubing over an aluminum ground plane.

The antenna shown in Fig. 2.11 is a stretchable RF antenna. The antenna consists of liquid metal (eutectic gallium indium alloy (EGaIn)) enclosed in elastomeric microfluidic channels.

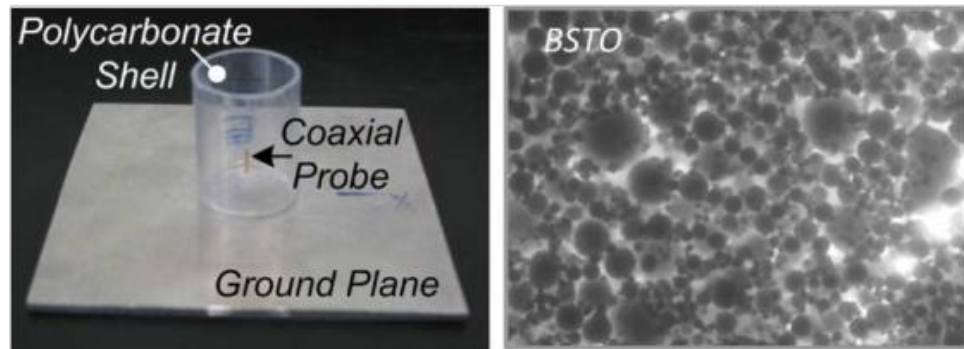


Fig. 2.10: Diagram of the coaxially fed DRA using colloidal dispersions.

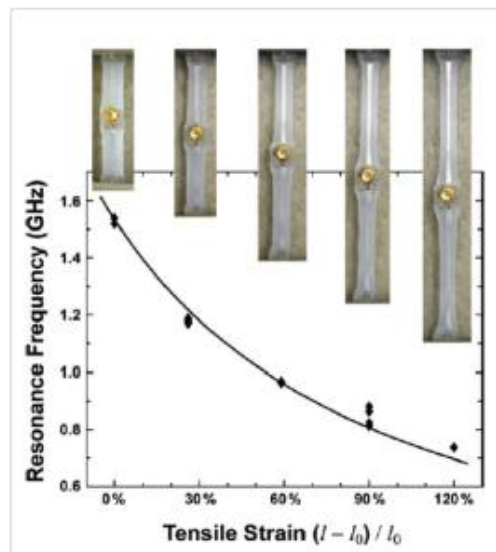


Fig. 2.11: Stretchable antenna.

## Chapter 3

### Digital Microfluidics

What we propose in this dissertation is to use Electrowetting on Dielectrics (EWOD) based Digital Microfluidics as a reconfiguration mechanism. This technique is distinctly different than prior art. A reconfigurable antenna, where its liquid elements can be actuated and moved in a controlled manner, for achieving dynamic reconfigurability in antenna properties was developed. Microfluidics deals with the behavior, precise control, and manipulation of fluids that are geometrically constrained to a small, typically sub-millimeter scale as a definition. Typically, micro means one of the following features:

- small volumes ( $nl$ ,  $pl$ ,  $fl$ ),
- small size,
- low energy consumption,
- effects of the micro domain.

#### 3.1 Continuous-Flow Microfluidics

These technologies are based on the manipulation of continuous liquid flow through microfabricated channels. Actuation of liquid flow is implemented either by external pressure sources, external mechanical pumps, integrated mechanical micro pumps, or by combinations of capillary forces and electrokinetic mechanisms. These systems are inherently difficult to integrate and scale because the parameters that govern flow field vary along the flow path making the fluid flow at any one location dependent on the properties of the entire system. Permanently etched microstructures also lead to limited reconfigurability. Therefore, following technique used as a reconfiguration mechanism for the designed antennas.

### 3.2 Digital (Droplet-Based) Microfluidics

Alternatives to the above closed-channel continuous-flow systems include novel open structures, where discrete, independently controllable droplets are manipulated on a substrate using electro wetting. Following the analogy of digital microelectronics, this approach is referred to as digital microfluidics. By using discrete unit-volume droplets, a microfluidic function can be reduced to a set of repeated operations, i.e., moving one unit of fluid over one unit of distance. Therefore, digital microfluidics offers a flexible and scalable system architecture as well as high fault-tolerance capability. Moreover, because each droplet can be controlled independently, these systems also have dynamic reconfigurability, whereby groups of unit cells in a microfluidic array can be reconfigured to change their functionality during the concurrent execution of a set of bioassays. One common actuation method for digital microfluidics is electrowetting-on-dielectric (EWOD). Many lab-on-a-chip applications have been demonstrated within the digital microfluidics paradigm using electrowetting. However, recently other techniques for droplet manipulation have also been demonstrated using Surface Acoustic Waves (SAW), optoelectrowetting, mechanical actuation, etc.

### 3.3 Electrowetting Theory

The basis of electrowetting can be traced back to G. Lippmans electro-capillary experiment in 1875. In this experiment, Lippman studied the effect of a potential difference applied to mercury inside a double-walled capillary tube. When a voltage was applied the interfacial surface tension of the mercury glass interface decreases causing the liquid to rise under the action of a capillary force. Lippman termed this process the electro-capillary effect. Later in 1976, Chudleigh and Minnema investigated the same effect using contact angle measurements on insulating polymer surfaces. In 1981, under the investigation of Beni and Hackwood, this phenomenon was given an official name of electrowetting. The true potential of electrowetting for display and optical applications was not truly realized until 1993 when Berge wrote an article on reversible electrowetting on dielectrics. Berge became known as the father of modern-day electrowetting techniques after writing this paper. Berge was the first scientist to apply a dielectric for electrowetting, which allows for



reversibility of the effect [49].

Electrowetting on dielectrics (EWOD) is a voltage-induced manipulation of small drops of polar liquids placed on a dielectric surface. In the presence of direct or alternating-current electric field, electrical charges gather together at the interface between conductive and dielectric material. If the interface is deformable like conductive or non-conductive liquid, electrical field induces an interfacial force that can create a distortion on the liquid which is called electrowetting [49]. The Young-Lippmann Eq. (3.1) explains electrowetting more specifically electrowetting on dielectrics (EWOD) - which aims movement of droplets on a solid substrate. The Young-Lipmann equation [49]:

$$\cos \theta = \cos \theta_0 + \frac{\epsilon_0 \epsilon V^2}{2\gamma_{LV}d}, \quad (3.1)$$

where  $\theta$  is the contact angle under applied voltage of  $V$  and  $\theta_0$  is the contact angle without externally applied potentials,  $\epsilon$  is the dielectric constant of a dielectric layer of thickness  $d$  and  $\epsilon_0$  is the vacuum permittivity. In Fig. 3.1, a small volume of an aqueous solution is deposited on a hydrophobic dielectric. The volume of liquid is limited so that the interfacial surface tensions dominate the shape of the droplet, thus outside effects, such as gravity, are greatly reduced. The basic electrowetting system can be modeled as a capacitor. A probe inserted into the aqueous solution together simulates the upper plate of a capacitor and is identified as the upper electrode. The electrode under the hydrophobic dielectric layer acts as a second capacitor plate and a base electrode. The term hydrophobic is defined as having a surface energy that allows the droplet to have an initial Youngs contact angle greater than  $90^\circ$ . Having the droplet at a voltage and the base electrode grounded an electric potential is introduced to the system. The electrowetting system can now be thought of as a capacitor where the dielectric is in between two electrodes, the droplet and electrode. In order to explain the electrowetting effect, Berge used a modified version of Lippmans equation by replacing the interfacial surface tension terms allowing  $\gamma_{SV}$  (solid-liquid) to reduce with increasing applied voltage (Fig. 3.2).

There are two critical parameters for EWOD design. Firstly, the initial contact angle

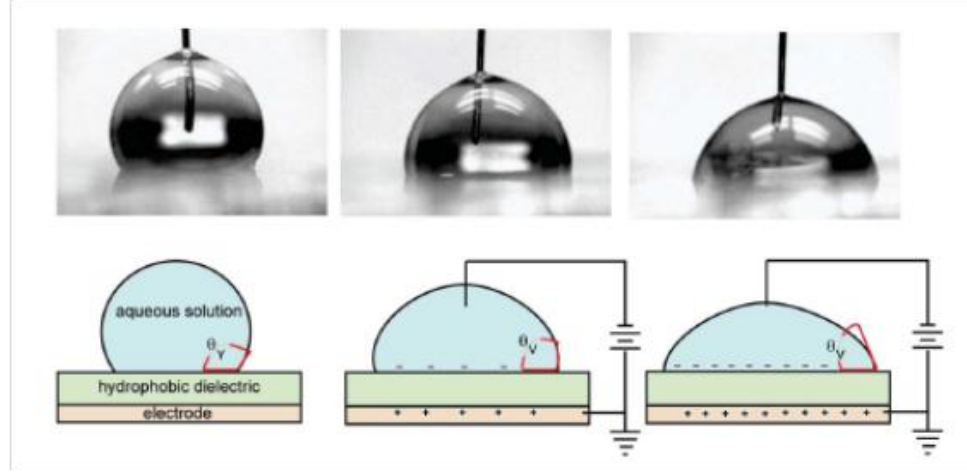


Fig. 3.1: The electrowetting effect in an air ambient. The left image illustrates the initial contact angle with no voltage applied, and the right image illustrates the new contact angle once a bias is introduced.

(without applied voltage) should be large enough to obtain a maximum contact angle variation; and secondly, the thickness of dielectric layer should be as small as possible to reduce applied potential [50]. However, minimum thickness should stand of applied voltage for the electrowetting effect before dielectric breakdown occurs. Mainly two different architectures have been developed for EWOD devices: open and covered systems (Fig. 3.3). In the open system, droplets sit freely on the top of the substrate; and for the closed system, droplets

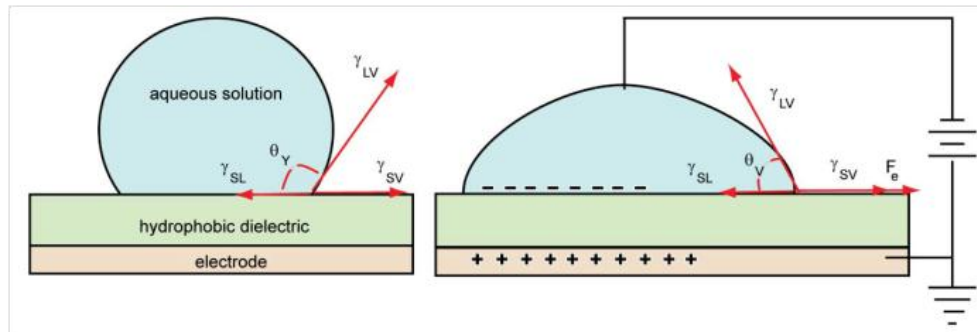


Fig. 3.2: Droplet on an ideal hydrophobic surface. In the left image, no potential is applied. In the right, a potential is applied between the substrate and polar liquid.

are confined between two plates.

Many droplet operations can be realized using either open or covered system designs. Independent from the architecture, these devices usually involve micro-fabricated metal electrodes on the top of the substrate. The electrode is coated by a dielectric layer and covered by a hydrophobic layer in order to increase the electrowetting effect on the droplet [50].

### 3.3.1 Electromechanical Model of EWOD

The derivation of the Lippmann law, i.e., the dependency of the contact angle according to the applied voltage, can be done by the following different approaches: the classical thermodynamic approach, the energy minimization approach, and the electromechanical approach. The first two approaches only address the static problem. If one wants to address the dynamic problem, which would require the inclusion of viscous effects, the forces exerted by the electric field on the interface have to be explicitly determined. Thereby, only electromechanical approach is given in details. The electromechanical interpretation of electrowetting presented throughout this section to demonstrate multiple points-of-view can be used to predict the macroscopic behavior of an observed physical phenomenon. In this analysis, the droplet is assumed to be a perfect conductor and the surrounding medium a perfect insulator.

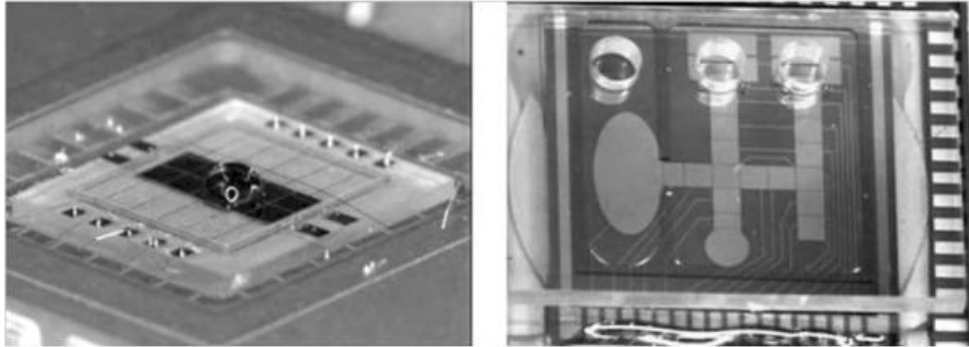


Fig. 3.3: Common electrowetting architectures (a) Open system (b) Covered system.

The electrostatic body force acting on a liquid is often formulated in terms of the Korteweg-Helmholtz body force density:

$$\overline{f_e} = \rho_f \overline{E} - \frac{\epsilon_0}{2} E^2 \nabla \epsilon + \nabla \left[ \frac{\epsilon_0}{2} E^2 \frac{\partial \epsilon}{\partial \rho} \rho \right], \quad (3.2)$$

where  $E$  is the electric field,  $\rho_f$  is volume density of free electric charge,  $\epsilon_0$  is permittivity in vacuum,  $\epsilon$  is the dielectric constant, and  $\rho$  is the mass density of the liquid. The third term on the right side of Eq. (3.2), known as electrostriction, is ignored since it has no influence on the hydrostatics as the mass density in a liquid remains constant [51]. Using the assumption that the liquid is a perfect conductor, the volume charge density in the liquid bulk is zero ( $\rho_f = 0$ ), but exists at the surface. The 2<sup>nd</sup> term on the right hand side of Eq. (3.2) is the ponderomotive force term, and as described by Jones [52], the ponderomotive force may appear to be nonphysical because there is no obvious mechanism for a dipole force at a boundary to exist when there is no electric field gradient, that is, no point-by-point body force distribution. However, this approach still works if you want to calculate the total force acting on the body not the distribution of forces acting within it. Therefore, the proper usage of Eq. (3.2) is to find the total force by taking the volume integral. Since the ponderomotive term force vanishes everywhere except at the surface, the net force can also be found by a surface integral. One of the implications of this argument is the total force acting on the body can be found by either a volume integral or equally appropriately by a surface integral of the Maxwell stress tensor.

Following classical electrodynamics, the conservation of momentum can be used to find the surface force by integrating along the surface of an element volume  $dV$  over the momentum flux density of the electric fields. This procedure produces the Maxwell stress tensor [53]. The Maxwell stress tensor consistent with Eq. (3.2) is:

$$T_{mn} = \epsilon_0 \epsilon \left( E_m E_n - \frac{1}{2} \delta_{mn} E^2 \right), \quad (3.3)$$

where  $\delta_{mn}$  is the Kronecker delta function and  $m, n = x, y, z$ . On the surface of a conductor

there is no tangential electric field [54]; thus the only non-vanishing component is the normal component which is related to the surface charge density by:

$$\rho_s = \epsilon_0 \epsilon \overline{E} \cdot \overline{n}. \quad (3.4)$$

The net force acting on a perfectly conductive liquid droplet is obtained by integrating over the interface surface:

$$F_m = \oint T_{mn} n_n dA, \quad (3.5)$$

where  $n_n$  is the outward unit normal vector. The force per unit surface area,  $\delta A$ , defined as electrostatic pressure and directed along the outward surface normal is:

$$\overline{F}/\delta A = P_{el} \overline{n} = \frac{1}{2} \epsilon_0 \epsilon E^2 \overline{n} = \frac{\rho_s \overline{E}}{2}. \quad (3.6)$$

To determine how this surface pressure affects the contact angle for a sessile drop requires solving for the electric field and charge density distribution along the surface of the drop. This is typically accomplished by solving the Laplace equation for an electrostatic potential,  $\nabla^2 V = 0$ , with appropriate boundary conditions. In practice, this is often achieved through a numerical analysis such as finite elements.

Both the field and charge distribution are found to diverge algebraically upon approaching the three phase contact line. This results in the Maxwell stress being a maximum at the contact line and decaying rapidly to negligible values at a distance equivalent to the dielectric thickness,  $d$ , from the contact line [55]. A schematic of the forces on the interface of a drop near the three phase contact line is shown in Fig. 3.4.

The schematic shown in Fig. 3.4 is the typically depiction of the liquid interface and contact angle formed due the electric field. However, this is an inaccurate portrayal. Recent research by Mugele confirmed that the local contact angle at the three phase interface remains equal to Youngs angle,  $\theta_Y$ , for the equilibrium drop condition (zero potential state), independent of the applied voltage. The distortions of the interface due to the electric field,

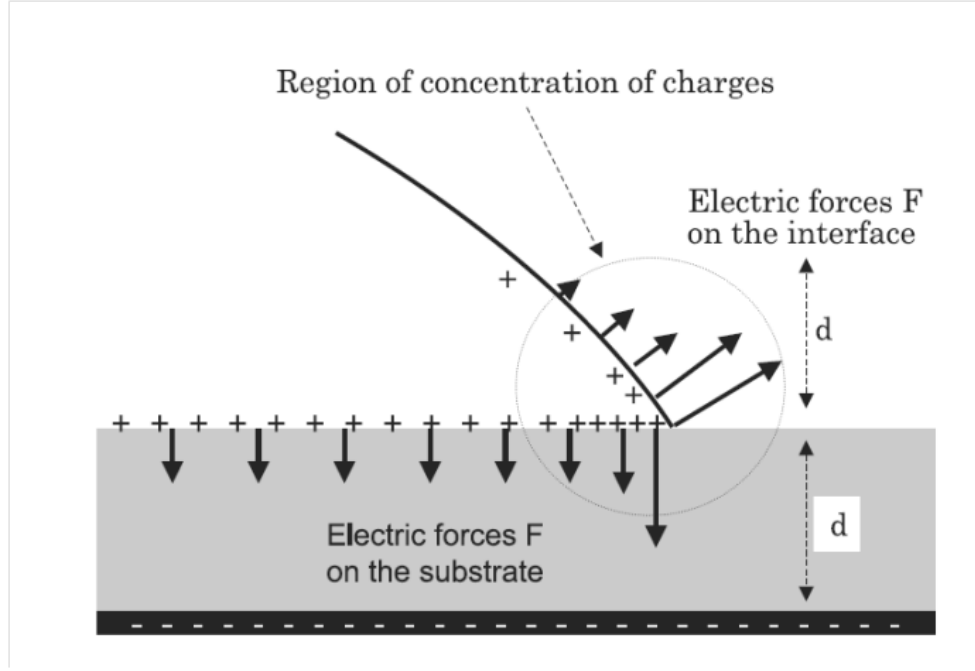


Fig. 3.4: Schematic of the electric charge distribution in the vicinity of the triple contact line. Electric charges are located at the solidliquid interface and at the liquidgas interface, approximately within a distance  $d$  from the solid surface. In reality, this is a very simplified view since the liquid interface is distorted by the electric forces very close to the triple contact line.

however, still occur on a scale of the dielectric thickness. Since the insulator thickness is typically on the order of microns or smaller the contact angle that can be measure and observed is equivalent to the contact angle predicted by the electrowetting equation, Eq. (3.1) and referred to as the Lippmanns angle,  $\theta_L$ . In general solving the Laplacian can be challenging because of the multi-dimensions involved with the problem. By using a conformal mapping procedure (the Schwarz-Christoffel mapping), there exist harmonic functions for  $E$  and  $V$  which allows Eq. (3.6) to be integrated. This transformation procedure treats the geometry near the three phase contact point as an infinite planar wedge [56].

The horizontal and vertical force components on the interface at the contact line are found to be:

$$F_x = \frac{\epsilon_0 \epsilon V^2}{2d}, \quad (3.7)$$

$$F_y = \frac{\epsilon_0 \epsilon V^2}{2d} \frac{1}{\tan \theta}, \quad (3.8)$$

where  $V$  is the applied potential,  $d$  is the dielectric thickness,  $\epsilon$  is the dielectric strength of insulator, and  $\theta$  is the contact angle. It is the horizontal force component that will pull on interface at the three phase contact line until it balances with the surface tension forces. The vertical component which does not contribute to the displacement of the interface is theorized by some researchers to play a role as a possible cause of contact angle saturation [51].

Given the rapid decay in the Maxwell stress from the three phase contact line and since the thickness of the dielectric layer is typically on the order of microns or smaller, while a size of a drop is on the order of millimeters in electrowetting systems, the electric static force in the macro sense can be considered to act as a point force at the three phase contact line. Because the horizontal force term in Eq. (3.7) can be represented as a point force, the equilibrium force balance at the three phase contact line, in conjunction with Youngs equation leads to:

$$\gamma_{wo} \cos \theta = \gamma_{so} - \gamma_{sw} + \frac{\epsilon_0 \epsilon V^2}{2d}. \quad (3.9)$$

This equation is identical to Eq. (3.1), the fundamental equation for electrowetting. In the macroscopic sense, the two methods are equivalent. An interesting aspect of Eq. (3.7) is it is independent of contact angle, which suggests the electrostatic force pulling on the interface is independent of interface shape, at least for the condition when the thickness of the dielectric layer is much smaller than the size of the drop. The implication of this is a change in contact angle is not the mechanism for translation of a drop but is the observed result of a net force exerted on the liquid due to a nonuniform electric field [51].

### 3.3.2 Limitations of EWOD

For ideal electrowetting to happen, all of the charge must stay in the conductive electrodes. Unfortunately, in the real world applications, there are effects that can limit the electrowetting performance of the devices. Two types of effects alter the final contact angle of the droplet: saturation phenomena and physical phenomena. Charging is the accumulation of charge in the dielectric layers. The accumulated charge neutralizes some of the charging found in the liquid electrode, thus reducing the force felt by the droplet. The accumulation of charging in the dielectric layers is most prevalent in two cases: when a static voltage is applied for an extended period and when a large voltage is applied to the system. Once a voltage is applied to the droplet for an extended period,  $> 1$  sec., the droplets contact angle will start to relax. The affect limits the capability of the minimum contact angle within the system and is coined saturation.

The next set of limiting phenomena is caused by the physical condition of the dielectric layer or by the ambient environment. Normally, when a droplet wets the surface, all of the oil is displaced from the bottom of the conductive liquid. In some cases, usually when a large bias is applied, oil can become trapped under the conductive electrode. These random small droplets increase the effective thickness of the dielectric limiting the electric field between the two electrodes at these sites. This will reduce the magnitude of the electric field based on the number of trapped droplets. Another limiting phenomenon, satellite droplets, occurs when a large bias is rapidly applied to the system. Sometimes a small amount of the conductive liquid can eject from the main droplet. These small droplets reduce the horizontal electric field around the edges of the larger droplet. While satellite droplets are more common in an air ambient, the affect can also occur in oil ambient. The final two limiting phenomena are actual physical properties of the coatings. In the first case, the fluoropolymer has delaminated from the dielectric exposing the dielectric. There are two problems with this case. First, the detached fluoropolymer creates a barrier, which restricts the movement of the droplet. Second, the dielectric from the fluoropolymer. This changes the initial contact angle of the system. In the final limiting phenomena, the fluoropolymer



surface has become fouled. If contamination is the cause, the sample is ruined. All of the aforementioned phenomena will limit the electrowetting response of the droplets. Usually, more than one of the listed limiting phenomena will determine the final contact angle.

## Chapter 4

### Tunable Zeroth-Order Resonator Antenna Based on EWOD

A new technology based on Electrowetting on Dielectrics (EWOD) for tuning the zeroth-order resonant frequency of a metamaterial transmission line unit cell has been demonstrated. The unit cell structure has been designed, fabricated, and characterized. The proposed structure eliminates complex biasing scheme by combining the Coplanar Waveguide (CPW) architecture with EWOD mechanism. EWOD phenomenon was exploited to expand the base contact area of a liquid mercury droplet placed on the unit cell, which resulted in changing the left-handed capacitance thereby tuning the resonant frequency. The main advantages of the proposed unit cell structure are its reliable operation with a simple structure and easy manufacturing processes needed to fabricate it. The design also offers flexibility where not only liquid metal but also liquid dielectric could be used. A new class of reconfigurable antennas could be realized by using this technology.

#### 4.1 Metamaterials

Metamaterials are synthesized structures whose electromagnetic properties can be engineered. The basis of a metamaterial is a unit cell that is much smaller than a wavelength. The individual properties of the unit cell aggregate to determine the effective material properties of the metamaterial as a whole. The design of the unit cell can be tailored to synthesize a variety of material parameters such as a positive or negative permittivity [57,58], a positive or negative permeability [59], a negative refractive index [60], or anisotropy [61]. This list of material parameters extends outside the realizable parameters found in nature. This leads to many interesting phenomena that can be realized such as, backward wave propagation, negative refraction, and sub-diffraction focusing. The unit cell itself can be repeated periodically or aperiodically, to form a homogenous or inhomogeneous metama-

material, respectively. Thus, at the heart of every metamaterial design is the unit cell which bestows the effective material properties on the metamaterial.

There are two main approaches that have arisen to synthesize metamaterials at microwave frequencies. They are the bulk approach and the transmission-line approach.

### Transmission Line Approach

Composite right/left-handed (CRLH) metamaterials are the metamaterials with both of the right-handed properties and the left-handed properties [62]. The CRLH metamaterials has been applied to some novel microwave devices. The properties of the CRLH metamaterials can be analyzed by the transmission line theory. The equivalent homogeneous (continuous and invariant along the direction of propagation) transmission line modes for the purely right handed (PRH), purely left handed (PLH), and CRLH transmission lines are shown in Fig. 4.1 [62].

As shown in Fig. 4.1, the PRH TL consists of a series inductance and a shunt capacitance, while the PLH consists of a series capacitance and a shunt inductance. The PRH TL actually does not exist because of the parasitic series inductance and the shunt capacitance. So the CRLH TL is more general than the PLH. The complex propagation constant  $\gamma$  of the transmission line can be expressed by:

$$\gamma = \alpha + j\beta = \sqrt{Z'Y'}. \quad (4.1)$$

The  $Z'$  and  $Y'$  are the impedance and the admittance per-unit length of the transmission line. For the case of CRLH transmission line, according to the circuit shown in Fig. 4.1, we can write:

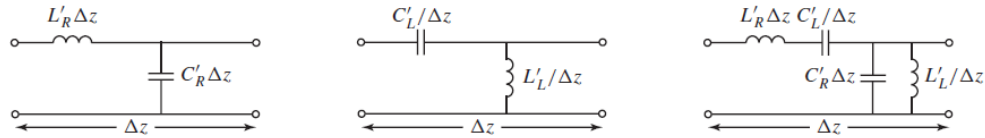


Fig. 4.1: Equivalent circuit models. (a) Homogeneous RH TL (b) Homogeneous LH TL (c) Homogeneous CRLH TL.

$$\begin{aligned} Z'(\omega) &= j\omega L'_R + \frac{1}{j\omega C'_L}, \\ Y'(\omega) &= j\omega C'_R + \frac{1}{j\omega L'_L}. \end{aligned} \quad (4.2)$$

Substituting Eq. (4.2) into (4.1), and assuming a lossless dielectric material ( $\alpha = 0$ ), one obtains:

$$\beta(\omega) = s(\omega) \sqrt{\omega^2 L'_R C'_R + \frac{1}{\omega^2 L'_L C'_L} - \left( \frac{L'_R}{L'_L} + \frac{C'_R}{C'_L} \right)}, \quad (4.3)$$

and

$$\begin{aligned} s(\omega) &= \begin{cases} -1, if \omega < \omega_{\Gamma 1} = \min \left( \frac{1}{\sqrt{L'_R C'_L}}, \frac{1}{\sqrt{L'_L C'_R}} \right) \end{cases}, \\ &\quad \begin{cases} -1, if \omega > \omega_{\Gamma 2} = \max \left( \frac{1}{\sqrt{L'_R C'_L}}, \frac{1}{\sqrt{L'_L C'_R}} \right) \end{cases}. \end{aligned} \quad (4.4)$$

The phase constant  $\beta(\omega)$  can be purely real or purely imaginary. When  $\beta$  is purely real, the electromagnetic fields will pass the CRLH transmission line without loss. If  $\beta$  is purely imaginary, then the CRLH is in a stop-band range because  $\gamma = j\beta$  is a real number.

It is well known that for the RH transmission line, the phase constant is given by:

$$\beta_R = \omega \sqrt{L'_R C'_R}, \quad (4.5)$$

and for the LH transmission line, we have [62]:

$$\beta_L = -\frac{1}{\omega \sqrt{L'_L C'_L}}. \quad (4.6)$$

Based on the Eqs. (4.3), (4.5), and (4.6), the dispersion diagrams for PRH TL, PLH TL, and CRLH TL are shown in Fig. 4.2 [62]. The  $\omega\beta$  diagram is called the dispersion

diagram.

## 4.2 Zeroth-Order Resonator

The CRLH TLs unique dispersion characteristic can be exploited to realize novel resonators not possible with conventional RH TLs. As a result, novel resonant antennas can also be realized by using CRLH TLs. To understand the unique resonance conditions of the CRLH metamaterial TL, a review of resonator theory is presented in this section. A conventional RH open- or short-circuited TL of physical length,  $L$ , can be used to realize a resonator with resonance condition described by:

$$\beta_n = \frac{n\pi}{L}, \quad (4.7)$$

where  $\beta_n$  is the phase constant of resonance mode  $n$  [63]. For the conventional TL resonator,  $n$  has to be a non-zero, positive integer. In the case of a CRLH TL resonator,  $n$  can be a positive integer, negative integer, or even zero. Figure 4.3(a) shows a CRLH TL of length,  $L = Np$  with its resonance modes shown in Fig. 4.3(b).

A CRLH TL of length,  $L = Np$  can support a total of  $2N - 1$  resonances:  $N - 1$  negative resonances,  $N - 1$  positive resonances, and a zeroth-order ( $n = 0$ ) resonance. The negative resonances have the same field distribution as the positive resonances, but at lower frequencies. By using the  $n = 1$  resonance of the CRLH TL resonator, a half-wavelength field distribution can be obtained at a much lower frequency than a conventional TL resonator of comparable length and substrate makeup. In the case of the  $n = 0$  resonance, an electrical length of zero is obtained. Therefore, the  $n = 0$  resonance is independent of the CRLH TL resonators physical length. For an unbalanced CRLH TL, there exist two possible  $n = 0$  resonances at  $\omega_{se}$  and  $\omega_{sh}$ . The  $n = 0$  mode for the unbalanced case is determined by the boundary condition applied to the input and output of the CRLH TL resonator. In the case of short-circuit boundary conditions, the shunt components of the CRLH unit cell are eliminated. Therefore,  $\omega_{se}$  determines the  $n = 0$  resonance for shortcircuit boundary conditions. The input impedance for short-circuit boundary conditions is given by:

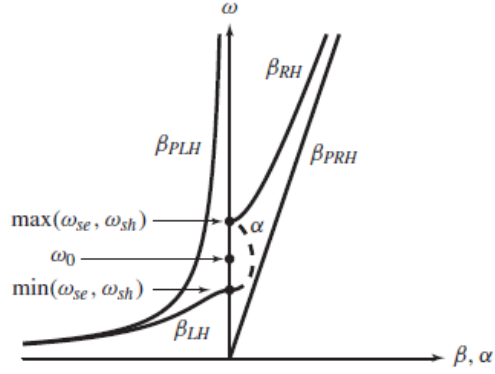


Fig. 4.2: Dispersion diagrams corresponding to the TLs.

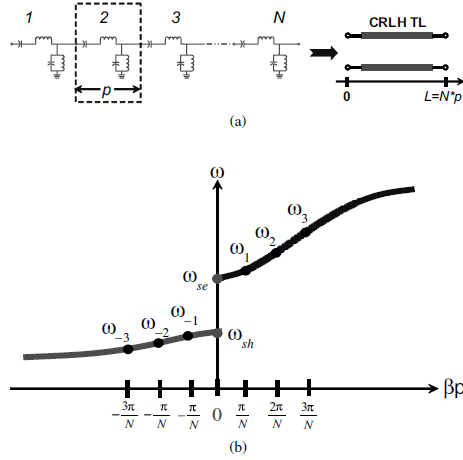


Fig. 4.3: Resonance modes corresponding to the TLs.

$$Z_{in,s.c.} = -jZ_0 \tan(\beta L) \stackrel{\beta \rightarrow 0}{\approx} -jZ_0 \beta L. \quad (4.8)$$

In the case of open-circuit boundary conditions, the series components of the CRLH unit cell are eliminated. Therefore, sh determines the  $n = 0$  resonance for open-circuit boundary conditions. The input impedance for the case of open-circuit boundary conditions is given by:

$$Z_{in,o.c.} = -jZ_0 \cot(\beta L) \stackrel{\beta \rightarrow 0}{\approx} -jZ_0 / \beta L. \quad (4.9)$$

In addition, the dispersive nature of the CRLH TL means that its resonance conditions are not harmonics of each other unlike a RH TL resonator. In general, the negative and zero resonance modes of the CRLH TL are of interest for antenna applications.

### 4.3 Tunable Zeroth-Order Resonator Transmission Line

A new approach for tuning the resonant frequency of metamaterial-inspired transmission lines (TLs) by using electrowetting on dielectric (EWOD) is presented in this section. Coplanar Waveguide (CPW) metamaterial-inspired TLs were designed and used as digital microfluidic platforms, where tunable resonance frequency was demonstrated for RF/microwave applications. A repeatable tuning mechanism was realized by exploiting the interface deformation of a liquid metal (mercury) droplet by an applied voltage. The maximum tuning range achieved is around 400 MHz (from 3.51 GHz to 3.92 GHz) with a DC actuation voltage of 110 V.

#### 4.3.1 Design

##### Capacitor Loaded Coplanar Waveguides

The CRLH TL has a particular aspect of supporting an infinite-wavelength wave at a finite and nonzero frequency defined as a zeroth-order resonance, which is solely dependent upon the series and shunt, inductances, and capacitances of the unit cell [64]. Equation (4.4) shows the equivalent circuit of a capacitor loaded TL unit cell, where the shunt inductance is removed eliminating the shunt resonance. This circuit supports the zeroth-order and positive resonances that can be tuned by adjusting the capacitor value (CL) as shown in Fig. 4.4.

In this work, a Coplanar Waveguide (CPW) was chosen as the host TL due to its uniplanar design and since it enables easy realization of the series and shunt connections of inductors and capacitors. Also, the coplanar electrode design makes it a particularly appropriate platform for an electrowetting actuation. The proposed CPW metamaterial-inspired TL can be modeled with the equivalent circuit shown in Fig. 4.4. The zeroth-order

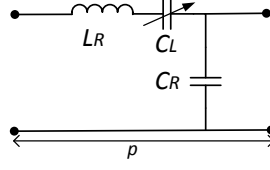


Fig. 4.4: Equivalent circuit of a capacitor loaded CPW.

resonant frequency occurs when the phase constant of Bloch wave along the structure equals zero,  $\beta = 0$ . The phase constant can be expressed in terms of the scattering parameters of the unit cell as given in Eq. (4.10). The proposed 2-port unit cell was also simulated by a full-wave analysis and measured in determining its scattering ( $S$ -) parameters. The propagation constant ( $\beta$ ) is then extracted from the measured scattering-parameters to determine the resonant frequencies [65].

$$\beta p = \cos^{-1} \left( \frac{1 - S_{11}S_{22} + S_{12}S_{21}}{2S_{21}} \right) \quad (4.10)$$

#### Tunable Zeroth Order Resonance Based on Electrowetting on Dielectric (EWOD)

The zeroth order resonant frequency of the proposed CPW metamaterial TL is  $L_R/C_L$  as is seen from the equivalent circuit shown in Fig. 4.4. Therefore, one can adjust the resonant frequency by changing  $C_L$  through the EWOD technique. A capacitor loaded CPW TL was used as an EWOD stage by simply adding a dielectric layer on the top of the TL metal layer. Figure 4.5 shows the unit cell geometry along with the dimensions of critical design parameters. This structure has an interdigitated finger like pattern which creates the left-handed capacitance,  $C_L$ , and also serves as the actuation electrodes for EWOD. The interdigitated section is covered by a Parylene/Teflon dielectric layer, on top of which a liquid metal (mercury) droplet is placed. Figure 4.6 depicts the cross section (A-A') view of the structure and also shows the EWOD phenomenon taking place. By using the EWOD phenomenon, this droplet is spread by DC actuation voltage applied between input and output ports of the structure as shown in Fig. 4.5 [66–68]. This movement of the liquid



metal droplet increases its base contact area, which in turn changes (increases) the effective left-handed capacitance,  $C_L$ . Thus the resonant frequency is changed (decreased) resulting in the desired tuning. The approach adopted in our design allows building low-cost and low-complexity tunable RF/microwave components with a simple bias network.

#### 4.3.2 Fabrication

Figure 4.6 is used to describe the microfabrication processes, where 4-inch Quartz wafer ( $\epsilon_r = 3.9$ ) with a thickness of 0.525 mm is used as a substrate material. For the metal layers of the CPW TL, a 20 nm Chromium (Cr), 200 nm Copper (Cu), 20 nm Cr, and 30 nm Nickel (Ni) metals were electron-beam (e-beam) evaporated successively and patterned by lift-off technique. This multi-layer metal also serves for the EWOD actuation electrodes. Ni was used to avoid reaction with mercury droplet, which is known to react with most of the metal materials. On top of the multi-layer metal, a 1  $\mu$ m thick dielectric layer of Parylene C was deposited at room temperature by vapor deposition, which was then patterned by reactive-ion-etch (RIE) using Oxygen ( $O_2$ ) plasma. In addition to Parylene C, another dielectric layer of hydrophobic Teflon AF with a thickness of 80 nm was spun coated to minimize contact angle hysteresis improving the robust repeatable operation. After coating, Teflon AF layer was baked at 200° C for 2 hours. Finally, this hydrophobic AF film was patterned by  $O_2$  plasma to define an opening of a circular-shape at the center, which was, subsequently, filled by an additional 20 nm/30 nm Cr/Au layer deposited by E-beam evaporation and patterned by lift-off. This circular pattern with a 100  $\mu$ m diameter at the center acts as an anchor providing a mechanical stability for the manually dispensed mercury droplet of 1 mm diameter [69]. In dispensing the droplets Gilson Microman micropipette was used. The photographs of a fabricated device are shown in Fig. 4.7. The manually dispensed mercury droplet has a volume of 1  $\mu$ L with a diameter of approximately 1 mm. After the applied voltage the mercury droplet spreads, which results in an increase of 150  $\mu$ m in the radius of the contact base area. The measured initial contact angle was 140° for the dielectric layer of Parylene C with a thin layer of hydrophobic Teflon AF on top. Some other dielectrics such as SU-8 and  $SiO_2$  were also used and tested, where Parylene C provided

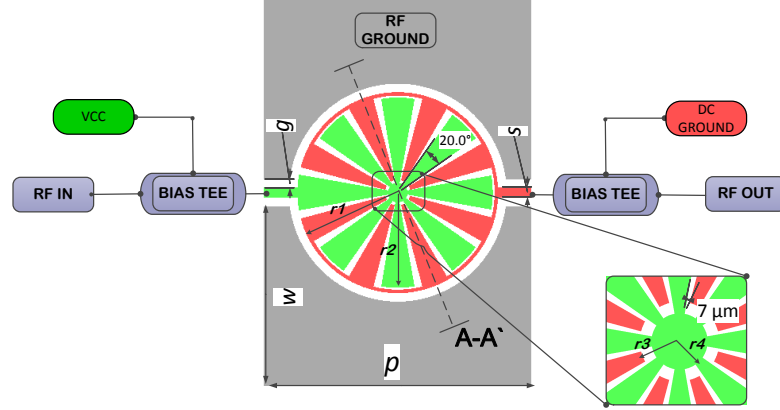


Fig. 4.5: The layout and test schematic of the tunable CPW metamaterial TL.  $p = 2$ ,  $w = 1.395$ ,  $s = g = 0.07$ ,  $r_1 = 0.75$ ,  $r_2 = 0.7$ ,  $r_3 = 0.1$ ,  $r_4 = 0.05$  (units in mm).

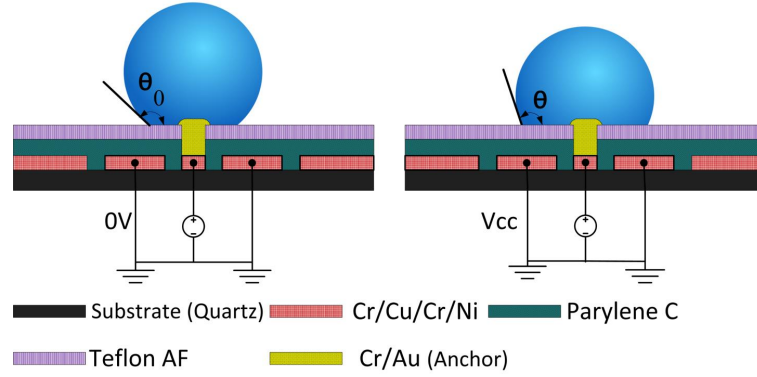


Fig. 4.6: Cross section (A-A') view of the structure and EWOD principle.

better frequency tuning with a robust repeatable operation. This shows that more contact angle change and less dielectric charging achieved by Parylene C.

#### 4.3.3 Experimental Results

The scattering parameter measurements of the fabricated CPW TLs have been performed by using Agilent 8722ES network analyzer with a 2-port Short Open Load Transmission (SOLT) calibration in the 50 MHz - 12 GHz frequency band. DC actuation voltage was supplied by a separate voltage source, which was applied to the terminals of RF input and output ports via bias tees as shown in Fig. 4.5. In this measurement set-up, the DC voltage

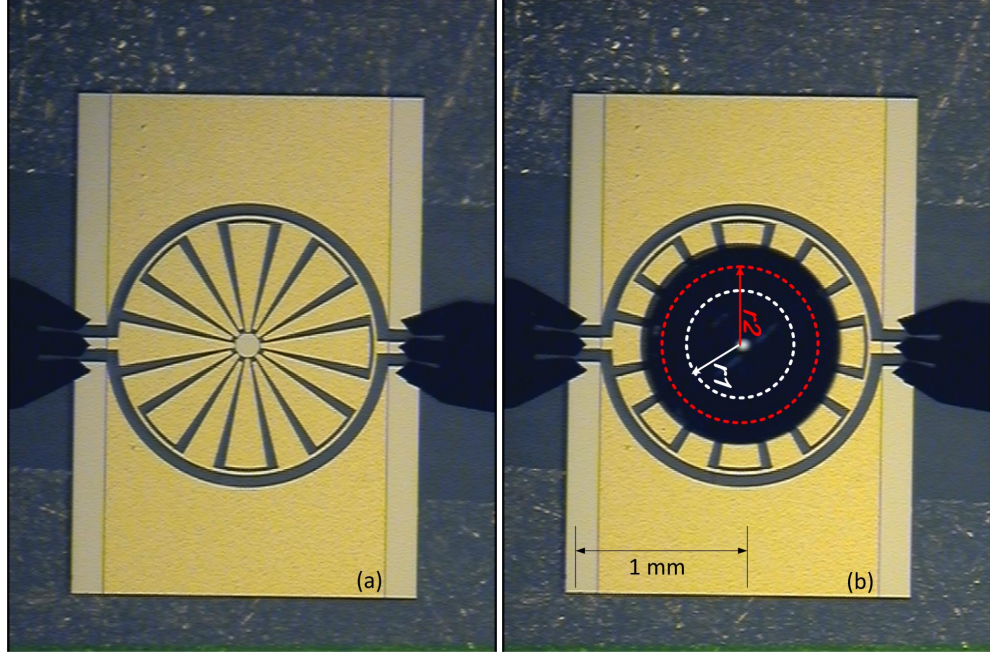


Fig. 4.7: The photographs of a fabricated device (a) before and (b) after mercury droplet dispensing. The boundaries of the base contact areas are illustrated with white and red dash lines before and after EWOD spreading, ( $r_2 - r_2 150\mu m$ ).

was superimposed with the RF source signal provided by the network analyzer, where the bias tees were used to prevent high DC voltages going into the network analyzer. In order to observe the reversible operation of the fabricated devices, the measurements started by applying the DC voltages in increments of 10 Vs (10 V, 20 V, 30 V  $\dots$  and 110 V), where the DC source was turned off at each step. We clearly observed that the spread mercury droplet returned back to its original non-spread stage every time the source was turned off. After obtaining the simulated and measured S-parameters of which variations with respect to frequency are given in Fig. 4.8(a,b), the dispersion behavior, which is represented by the variation of phase constant as a function of frequency has been obtained by using Eq. (4.10). As shown in Fig. 4.8(c), the zeroth-order resonance frequency was shifted from 3.92 to 3.51 GHz by the applied DC voltage of 110 V providing a maximum tuning range in excess of 400 MHz. The actuation voltages above 110V cause the mercury droplet to be freed from the anchor thereby the droplet starts moving. As the device operation relies

on the spread of the droplet while it is fixed at the central anchor location, the normal device operation mechanism is lost above 110V. Slight variations in the RF responses from device-to-device on the wafer were also observed, which could mainly be attributed to the small variations in the hand dispensed volume.

The main advantages of the proposed unit cell structure are its reliable operation with a simple structure and easy manufacturing processes needed to fabricate it. The design also offers flexibility where not only liquid metal but also liquid dielectric could be used. A new class of tunable phase shifters, antennas, and microwave filters could be realized by using this digital microfluidic platform as building blocks.

#### 4.4 Antenna Application

In this section, the  $n = 0$  resonance mode supported by a capacitor loaded CPW TL resonator is used to realize infinite wavelength resonant antennas with monopolar radiation patterns with the concept introduced last section. The infinite resonant antenna can be made arbitrarily small and single droplet could be used for reconfiguration. In the case of short-circuit boundary conditions, the resonant frequency is determined by the series resonance of the unit cell. More unit cells can also be used to enhance the directivity of the proposed antenna. Capacitor-loaded CPW is short-circuited through a short section of CPW line of relatively higher characteristic impedance. This CPW section is needed to compensate for the degradation of the input matching condition at the series resonance when fewer unit cells are used.

The antenna (Fig. 4.9) simulated using Agilent ADS and Ansys HFSS to confirm that the antenna works as intended and to get a better understanding of the antenna parameters such as  $S_{11}$ , input impedance, current density distributions, radiation patterns, and efficiency. Since the same dimensions used as previous section, tuning range and center frequency is same with the transmission line examples. Only difference is the antenna is a one port device and needs the matching circuit. The antenna has disadvantages as any other metamaterial antenna like the low efficiency and small bandwidth.

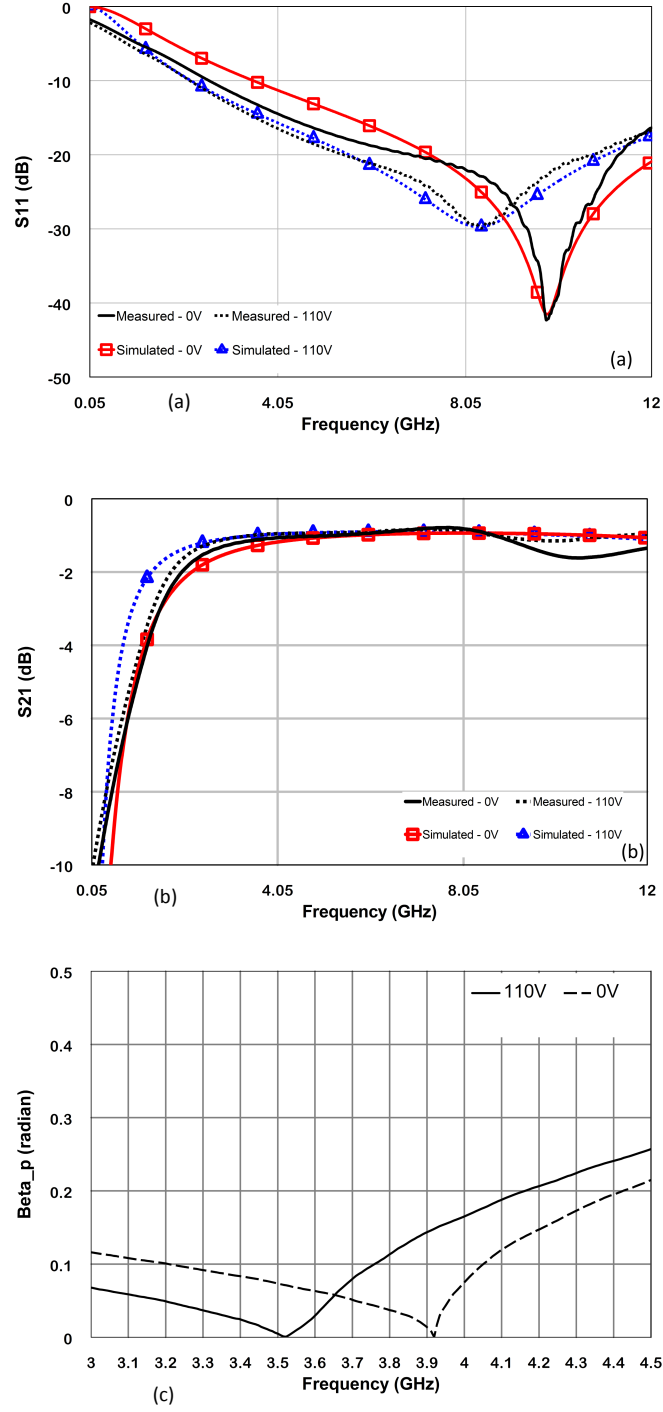


Fig. 4.8: Simulated and measured (a) S11 (b) S21 parameters before and after applied voltage of 110 Volts (c) Calculated propagation constant of the unit cell structure.

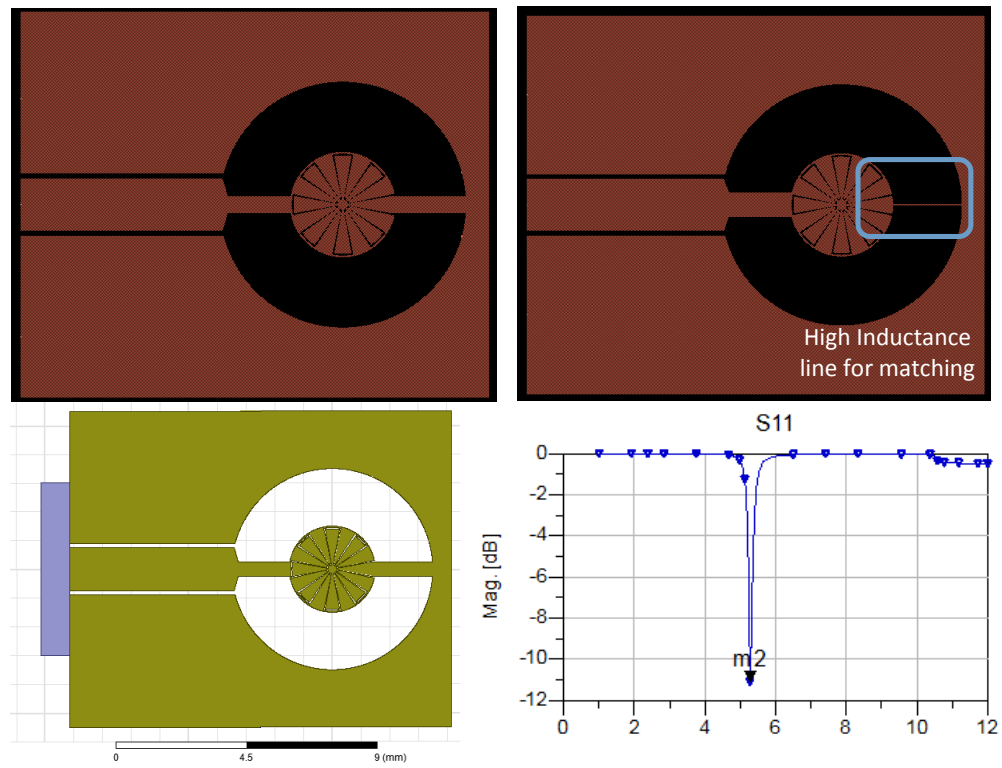


Fig. 4.9: ADS and HFSS models of the proposed antenna and reflection coefficient after matching.

## Chapter 5

### A Frequency Reconfigurable Antenna Based on EWOD

We present a novel antenna reconfiguration mechanism relying on electrowetting-based digital microfluidics to implement a frequency reconfigurable antenna operating in the X band. The reconfigurable antenna built on a quartz substrate ( $\epsilon_r = 3.9$ ,  $\tan \delta = 0.0002$ ) is a coplanar waveguide (CPW) fed annular slot type antenna, which is monolithically integrated with a microfluidic chip. This chip establishes an electrowetting on dielectric (EWOD) platform with a mercury droplet placed in it. The base contact area of the mercury droplet can be spread out by electrostatic actuation, thereby resulting in a change of loading capacitance. This in turn changes the resonant frequency of the antenna enabling a reversible reconfigurable impedance property. This reconfigurable antenna has been designed, fabricated, and measured. The frequency of operation is tuned from around 11 GHz to 13 GHz as demonstrated by simulations and measurements from the fabricated prototypes. The design methodology, fabrication processes, and the experimental results are given and discussed.

#### 5.1 Design and Working Mechanism

The presented digital microfluidic-based MRA introduces new design requirements as the EWOD platform and the liquid metal are the integral parts of the radiating antenna structure directly impacting its performance characteristics (radiation and impedance properties). Therefore, an integrated design approach, where the electromagnetic (EM) and digital microfluidics related parameters are jointly optimized, must be adopted.

Choosing the proper liquid material is crucial as this material must be compatible with both EWOD mechanism and EM performance of the antenna. Although the liquid metals and dielectrics have been both demonstrated for the antenna applications, the dynamic

manipulation of liquid metals by EWOD plays an important and distinguishing role in the presented MRA case. Most of the current EWOD applications are focused on the dielectric liquid manipulation, which might not be suitable for high-frequency applications, due to the high dielectric losses. Therefore, liquid metal, of which conductivity is similar to that of solid metals such as copper (Cu), gold (Au), etc., becomes the preferred option. There are only few metals available in liquid form at the room temperature. Mercury being one of them has been used for RF switching applications by EWOD because of its widespread availability even though it has a toxic nature. Recently, non-toxic room temperature liquid metal alloys, such as Galinstan, have also been available. However, the necessity of controlling the thin oxide layer formation due to its sensitivity to air exposure presents significant challenges for successful EWOD actuation. For these reasons, the presented MRA uses mercury as the liquid metal for EWOD actuation.

Figure 5.1 shows the 3-D schematic of the MRA with an inset showing the magnified view of the integrated microfluidic chip. As seen from this figure, the basic antenna structure is a coplanar waveguide (CPW) fed annular slot antenna built on a quartz substrate ( $\epsilon_r = 3.9$ ,  $\tan \delta = 0.0002$ ) with a thickness of 1 mm. For the permittivity value of the quartz substrate, the slot guided wavelength,  $\lambda_g$  at the resonant frequency can be given as below:

$$\frac{\lambda_g}{\lambda_0} = 0.9217 - 0.277 \ln \epsilon_r + 0.0322 \frac{W}{h} \left[ \frac{\epsilon_r}{W/h + 0.435} \right]^{1/2} - 0.01 \ln \frac{h}{\lambda_0} \left[ 4.6 - \frac{3.65}{\epsilon^2 (9.06 - 100 (W/\lambda_0)) \sqrt{W/\lambda_0}} \right], \quad (5.1)$$

where  $W = r_1 - r_2$  is the slot-line width (see (Fig. 5.1)),  $\lambda_0$  the free-space wavelength,  $\epsilon_r$  and  $h$  are the permittivity and thickness of the quartz substrate, respectively. While Eq. (5.1) provides a good first-order approximation for the resonance frequency, the actual frequency for the digital microfluidic annular slot antenna will be in the close vicinity of that of given by Eq. (5.1). This is due mainly to the microfluidic chip, which is integrated within the basic annular slot antenna, where the RF ground line is extended into the micro-chamber



structure as can be seen from Fig. 5.1. By using Eq. (5.1) as a first order approximation in conjunction with full-wave EM analyses, the dimensions of the antenna and CPW of 50 characteristic impedances along with the transition regions have been determined for the targeted X band operation (center resonance 12 GHz), and are given in the caption of Fig. 5.1.

As seen from Fig. 5.1, the microfluidic chip which consists of SU-8-based cylindrical micro-chamber, micro-frames (4 columns), and EWOD platform with a mercury droplet placed in it is located at the right side of the MRA center. In order to precisely control the dispensing, positioning, and the spreading of the mercury droplet by EWOD, it is confined within the micro-frame structure, which also serves to avoid undesired gravitational effects. Moreover, a circular chamber design was used to house silicone oil droplet, which encapsulates the mercury droplet. This silicone oil serves for reducing actuation voltage for spreading the mercury droplet by EWOD, reduces the uncertainty due to contact-angle hysteresis, and also provides the initial structure for ultimate packaging. The volume of the mercury droplet has been so determined ( $1\mu L$ ) that not only the RF capacitive loading required for the desired frequency tuning range ( $\approx 2GHz$ ) but also a simple EWOD platform can be obtained (see Appendix). Accordingly, the associated dimensions corresponding to these design features have been determined by full-wave EM analyses and are given in the caption of Fig. 5.1. As shown in Fig. 5.1, the RF ground and signal planes comprise the EWOD electrode. The dispensed mercury droplet sits on the Parylene dielectric layer, which is deposited on top of the high resistive TaN layer. Notice from the upper inset of Fig. 5.1 that there is an opening of a circular shape at the center, which provides the DC contact between the mercury droplet and the RF ground metal required for the EWOD actuation. The additional high-resistive layer is needed to increase the loading capacitance,  $C_l$ , which can be given as:

$$C_l = C_{on} - C_{off}, \quad (5.2)$$

where  $C_{off}$  and  $C_{on}$  are the coupling capacitances before and after spreading by EWOD,

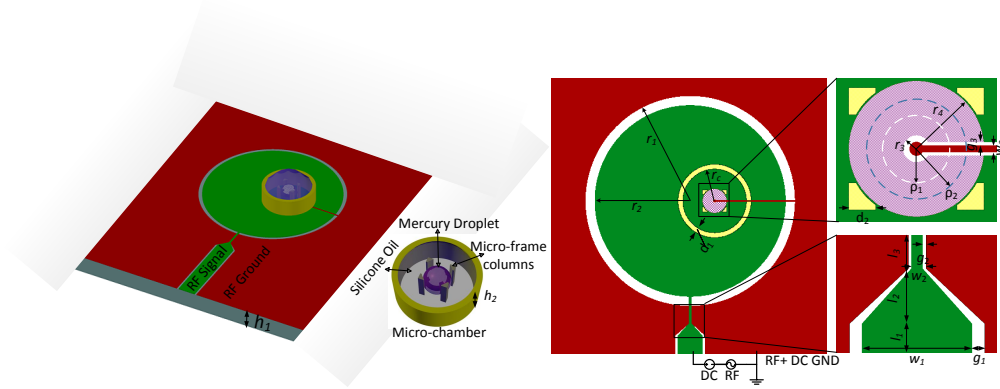


Fig. 5.1: (a) 3-D schematic of the MRA integrated with a microfluidic chip. The inset shows the magnified view of the microfluidic chip; (b) Top view of the MRA with magnified views of the CPW feed and EWOD platform (1 and 2 are the radii of the contact base area of Mercury droplet, before and after spreading). The design dimensions are:  $r_1 = 4.1, r_2 = 3.9, r_c = 1.3, r_3 = 0.1, r_4 = 0.5, w_1 = 1, w_2 = 0.1, w_3 = 0.05, g_1 = 0.015, g_2 = 0.0115, g_3 = 0.025, l_1 = 4.5, l_2 = 0.45, l_3 = 0.7, d_1 = d_2 = 0.2, h_1 = 1, h_2 = 1, 1 \cong 0.320, 2 \cong 0.470$  (units in mm).

respectively. The loading capacitance is responsible in providing the desired frequency tuning range of  $\approx 2GHz$ . It is important to note that the capacitive coupling occurs due to the mutual coupling between the mercury droplet and RF signal plane. To spread the mercury droplet by EWOD technique, a DC actuation signal of  $\approx 140V$ , which is superimposed on the RF signal, is applied to the CPW signal and ground planes as shown in Fig. 5.1. Thus, the contact base area of the mercury droplet is spread outwardly, which brings it closer to the RF signal plane, thereby increasing the coupling capacitance. The upper inset of Fig. 5.1 also shows the edges of the contact base area before and after EWOD operation ( $\rho_1$  and  $\rho_2$ ). As is seen from this figure, the lateral spreading of  $150 \mu m$  ( $\rho_2 - \rho_1$ ) provides a large enough loading capacitance resulting in the desired frequency tuning as demonstrated by simulations and measurements. Notice that the CPW RF feed design enables the signal and ground metallization of the antenna to be also used for EWOD actuation electrodes, thereby resulting in a simple biasing network.

## 5.2 Fabrication

A proof of concept frequency reconfigurable antenna that is designed to reconfigure its central operating frequency from 11 GHz to 13 GHz, have been fabricated and measured. Figure 5.2 shows two different cross section views (AA' and BB') and the corresponding microfabrication process flows.

The process starts with the deposition of a 200 nm thick Tantalum Nitride (TaN) with a sheet resistivity of 700 ohm/sq on a 4-inch quartz substrate of 1 mm thickness. The TaN layer was deposited by reactive sputtering and patterned lithographically using a reactive ion etching. For the antenna and CPW metal layers a 20 nm Chromium (Cr), 1000 nm Copper (Cu), 20 nm Cr, and 30 nm Nickel (Ni) were electron-beam (e-beam) evaporated successively and patterned by lift-off technique. Ni was used to avoid reaction with mercury droplet, which is known to react with most of the metals. On top of this multilayer metal, a 1mm thick dielectric layer of Parylene C was deposited at room temperature by vapor deposition, which was then patterned by reactive-ion-etch (RIE) using Oxygen ( $O_2$ ) plasma. Next, the micro-frame structure of four columns and the micro-chamber were formed by processing SU-8 material. The height of SU-8 columns and the chamber with 1 mm thickness was determined by the typical diameter (1 mm) of the mercury droplets. A deposition process was developed in order to obtain such an ultra-thick structures with a single spin of SU-8 2100 (Microchem). To increase the adhesion of these structures to antenna metal layer, OmniCoat (Microchem) (adhesion promoter for SU8) was used. In this developed process, 12 mL of SU-8 2100 was spun with 500rpm coating speed. The temperatures for the soft and post-exposure baking are also critical process parameters, which were determined to be 120°C and 55°C, respectively. Moreover, the baking temperatures were always ramped up and down with a rate of 1°C/min from 50°C. This prevents the ultra-thick SU-8 structures from cracking and distorting during developing and baking processes. Also, a step exposure with each step consisting of a 60 s exposure and a 30 s delay was used. After post-exposure bake, the micro-frame and micro-chamber features were developed with slow agitation. Finally, a mercury droplet of a 1 mm-diameter was placed in each micro frame manually. In dispensing the

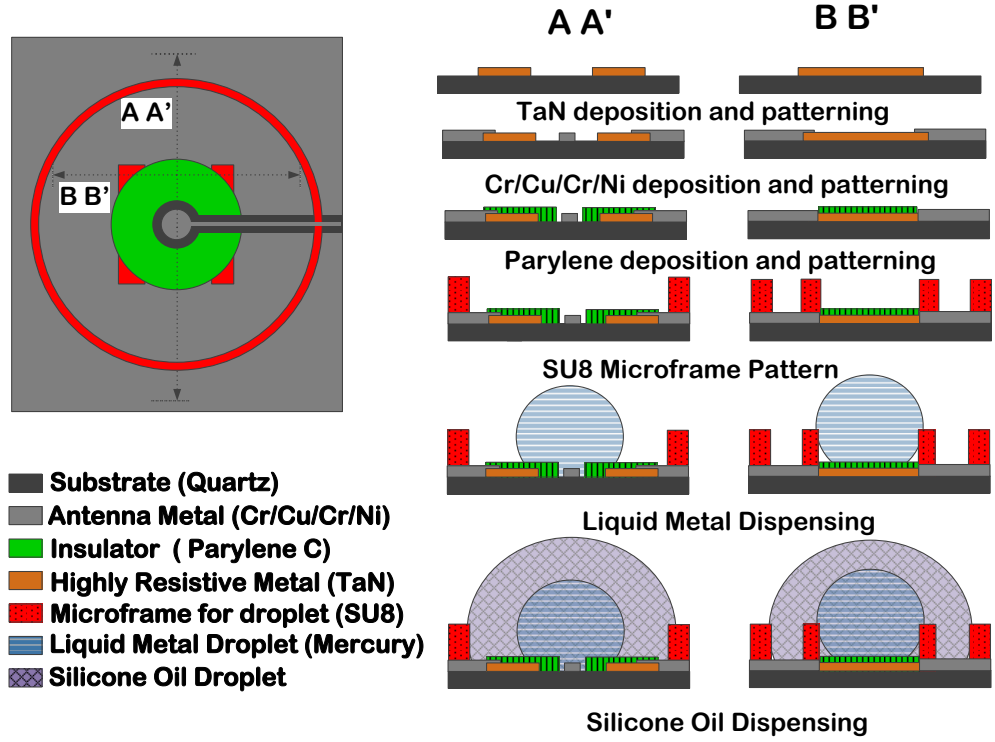


Fig. 5.2: The process flow for fabricating the frequency reconfigurable antenna integrated with a microfluidic chip.

droplets, Gilson Microman micropipette was used. After dispensing the mercury droplet, micro-chamber was filled with silicone oil encapsulating the mercury droplet as shown in the last step of Fig. 5.2. Figure 5.3 shows a top-view photograph of a fabricated MRA prototype. The pictures of an empty, mercury filled, and mercury and silicone oil filled microfluidic chips are shown, respectively.

### 5.3 MRA Prototype Characterization

The frequency response of the fabricated frequency reconfigurable antenna prototype has been measured and the measured results were compared with those of the simulated results. To perform the RF measurements, a 3.5 mm SubMiniature version A (SMA) RF connector was attached to the input port of the CPW feed line by using a conductive epoxy, as shown in Fig. 5.3. The prototype was then connected to a fully-calibrated single port of a

vector network analyzer (VNA). To spread the mercury droplet by EWOD, a DC actuation voltage ( $V_{cc}$ ) was supplied by a separate voltage source, which was superimposed with the RF source signal provided by the VNA (see Fig. 5.1). The total signal was applied to the CPW feed line via bias tees, which are used to prevent high DC voltages going to the VNA. The results for antenna reflection coefficients are shown in Fig. 5.4, where the tuning in frequency in response to the spread of the mercury droplet is clearly observed. When the mercury droplet is in its un-actuated state ( $V_{cc} = 0V$ ), the center frequency of operation is at around 13 GHz as confirmed by both from measurements and simulations shown in Fig. 5.4. An applied DC actuation voltage of  $\approx 140V$  causes the mercury droplet to spread, which in turn increases the loading capacitance, thereby resulting a shift in the frequency of operation, which brings it to 11 GHz range. A reasonably good agreement between the measured and simulated results demonstrates the robustness of the fabricated prototype and the accuracy of the design methodology.

The integrity of the radiation properties (gain values and shape of the radiation pattern) of the reconfigurable antenna is maintained over the reconfigurable frequency band (11 to 13 GHz) as demonstrated by the full-wave simulations. Maintaining the characteristics of one parameter, which in this case are the radiation properties, while reconfiguring another parameter (frequency) is an important design requirement for reconfigurable antennas.

As a conclusion, a new class of frequency reconfigurable antenna integrated with a microfluidic chip has been designed, micro-fabricated, and measured. This reconfigurable antenna uses EWOD mechanism to manipulate the contact base area of a liquid metal mercury droplet, which in turn changes the frequency of operation from 13 GHz to 11 GHz, thus achieving reconfigurability in frequency of operation. The microfabrication processes relying on ultra-thick (1 mm) SU-8 have also been developed in order to build and monolithically integrate the microfluidic chip. The reflection coefficient results showing the frequency reconfigurability were successfully demonstrated both theoretically and experimentally. This reconfigurable antenna, which uses only a single mercury droplet as a main building block in a microfluidic chip, will pave the way of more sophisticated MRAs integrated with a

microfluidic chip having multiple mercury droplets, where spreading, moving, merging, and splitting operations can be performed. Such an MRA results in more advanced reconfigurable functions simultaneously in frequency, radiation pattern, and polarization, which are critically needed for the next generation cognitive wireless communication applications.

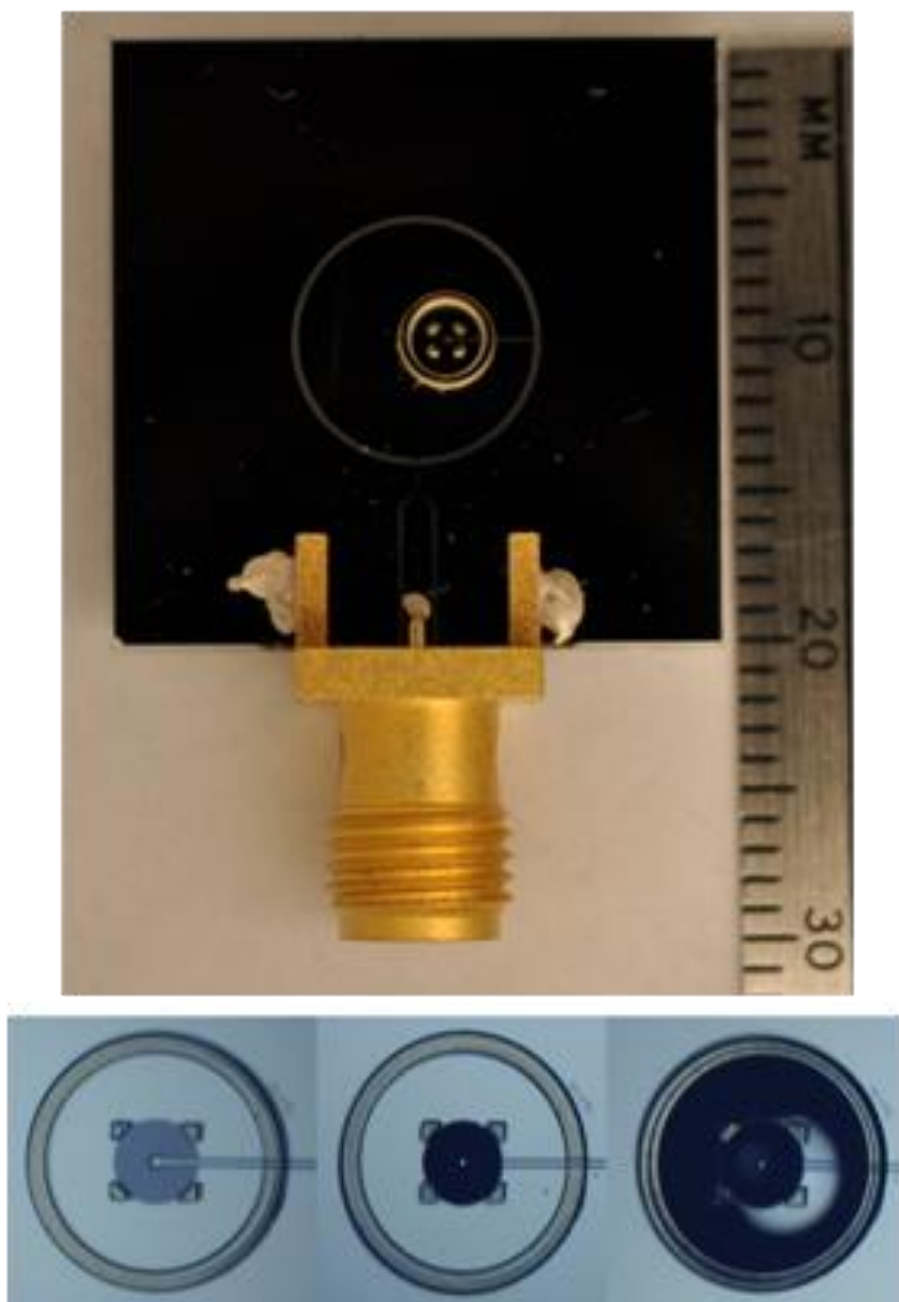


Fig. 5.3: The photographs of (a) the top view of a fabricated MRA prototype; and (b) an empty, mercury filled, and mercury + silicone oil filled microfluidic chips.

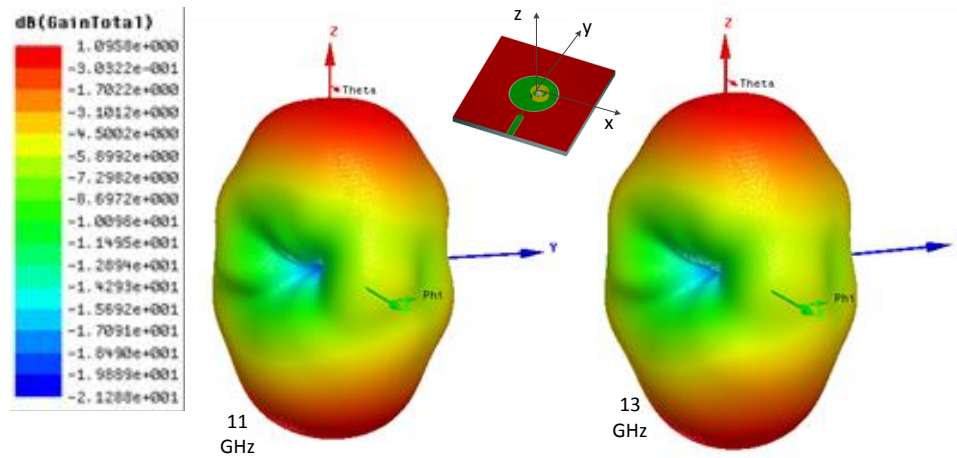
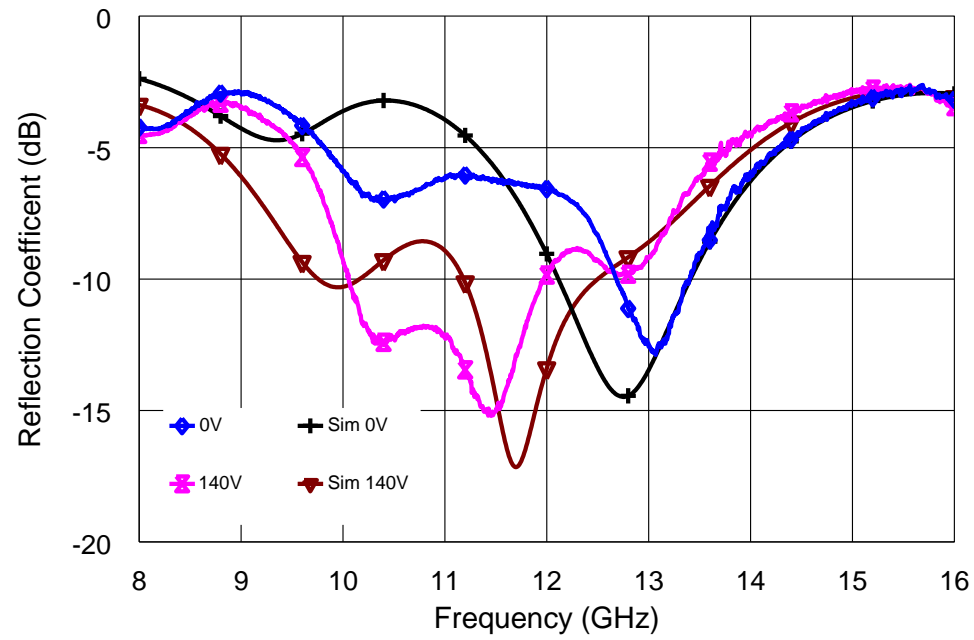


Fig. 5.4: Measured and simulated reflection coefficients and radiation patterns corresponding to  $f=11$  GHz (ON state) and  $f=13$  GHz (OFF state) modes of operations.



## Chapter 6

### RF Switch Based on Reversible Wetting States on Superhydrophobic Surfaces

A new way to build a tunable component using superhydrophobic micro-structured surfaces are introduced in this chapter. Liquids tend to bead up in droplets on such surfaces rather than forming a continuous wetted surface. These surfaces, along with tunable wetting techniques can be used for creating novel RF devices such as reconfigurable antennas.

Based on microfabrication techniques, we have created a variety of microstructured superhydrophobic surfaces with precisely controlled morphology and chemical functionalization. Liquid metal droplets, such as mercury, placed on these surfaces exhibits very large contact angles, a high level of mobility, and small contact angle hysteresis. Using electric fields, reversible transitions between the wetted and superhydrophobic have been investigated for RF switching applications.

#### 6.1 Superhydrophobic Surfaces

Superhydrophobic surfaces have important applications in the development of artificial self-cleaning surfaces and water-proof clothing. They also find use in microfluidic-based technologies such as lab-on-chip devices, microelectromechanical systems (MEMS), and microarray biochips. Lotus leaves are known for their water repellency and consequently to remain clean from any parasitic dust or debris. This phenomenon (also called rolling ball state) is very common in nature not only for the lotus, but also for nearly 200 other species: vegetables, insects, and even some animal species. Figure 6.1 shows a typical Scanning Electron Microscope (SEM) picture of a Lotus leaf.

The common point between all water repellant surfaces is their roughness in combination with low surface energy chemistry. Indeed, the surfaces are composed of micrometric

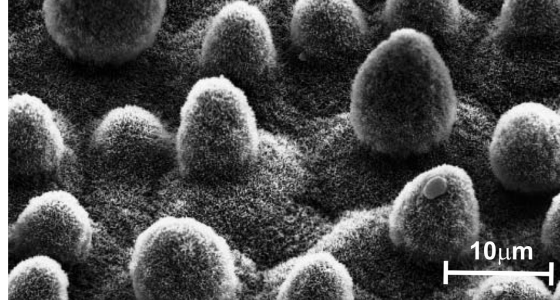


Fig. 6.1: SEM image of a Lotus leaf.

structures limiting the impregnation of the liquid and pushing back the drop. Most of the time, the surfaces contain a second scale of roughness, consisting of nanometric size [70,71]. In order to minimize its energy, a liquid droplet forms a liquid pearl on the microstructured surface. The superhydrophobicity term is thus used when the apparent contact angle of a water droplet on a surface reaches values higher than  $150^\circ$ . Previously, the studied substrates were regarded as smooth surfaces, i.e., the roughness of the substrate was sufficiently low and thus does not influence the wetting properties of the surface. In this case, the relation of Young gives the value of the contact angle  $\theta$  on the surface. However, a surface can have a physical heterogeneity (roughness) or a chemical composition variation (materials with different surface energies). A new contact angle is then observed, called the apparent contact angle noted  $\theta^*$ . It should be noticed that locally, the contact angle between the liquid droplet and the surface can assume almost any value with these geometries due to pinning of the contact line. Two models exist which describe the enhancement of the apparent contact angle: the model of Wenzel and of Cassie-Baxter (Fig. 6.2).

Drop on a rough and hydrophobic surface can adopt two configurations: (a) a Cassie-Baxter configuration (air patches are confined below the drop), and (b) a Wenzel [71] (solid/liquid interface exactly follows the solid roughness). In both cases, an increase in the apparent contact angle of the drop is observed. These two models were highlighted by the experiment of Johnson and Dettre. Many research teams have tried to understand in more detail the superhydrophobicity phenomenon and particularly the difficulty of the wetting transition from the Wenzel to Cassie configuration [72]. For a superhydrophobic surface, a

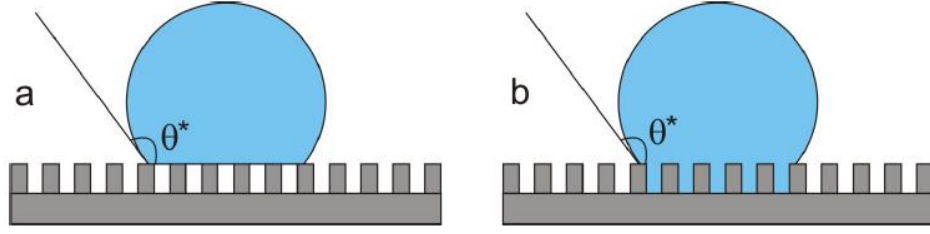


Fig. 6.2: Superhydrophobic surfaces (a) Cassie-Baxter (b) Wenzel states.

pronounced difference between the two models is the hysteresis value. The first experiment on this subject was conducted by Johnson and Dettre (1964) who measured the advancing and receding contact angles, according to the surface roughness. For low roughness, a strong hysteresis, up to 1000 (Wenzel), is observed and attributed to an increase in the substrate surface in contact with the drop. Starting from a certain roughness (not quantified in their experiment), the hysteresis becomes quasi null resulting from the formation of air pockets under the drop (Cassie-Baxter state). The receding angle approaches the advancing angle. Other experiments also show that for a drop in the Cassie-Baxter state, it is possible to obtain a contact angle significantly higher than for a drop in the Wenzel state.

The apparent contact angle of a sessile droplet in the Cassie ( $\theta_c$ ) and Wenzel ( $\theta_w$ ) states may be obtained using energy minimization and is given by:

$$\cos \theta_c = (-1 + \phi (1 + \cos \theta_0)), \quad (6.1)$$

$$\cos \theta_w = r_m \cos \theta_0, \quad (6.2)$$

where  $\phi$  is the ratio of the area of the top surface of the pillars to the total base area of the substrate,  $r_m$  is the surface roughness, defined as the ratio of the total surface area (including the sides and base) of the roughness elements to the projected surface area (not including the sides of the roughness elements).  $\theta_0$  is the contact angle of the droplet on a flat surface. The equations are not valid for high roughness.

## 6.2 Switching of Wetting States on Superhydrophobic Surfaces

Superhydrophobic surfaces display remarkable properties including ultrahigh contact angles, ultralow contact angle hysteresis, large hydrodynamic slip, and tunable optical diffraction. These properties rely on the weak interaction between the liquid and the substrate due to the entrapment of air (or vapor) in the cavities of the rough surface topography. At the transition from the superhydrophobic Cassie state to the normal Wenzel wetting state, the gas from the cavities is expelled and the interaction between the liquid and the substrate increases dramatically. The contrasting properties of the Cassie and the Wenzel state make it particularly attractive to design surfaces that allow for switching between the two wetting states. Various external control parameters have been used to trigger the transition from the Cassie to the Wenzel state, including hydrostatic pressure, optical, and chemical stimuli [73], as well as electric fields. In particular, the latter offers opportunities for fast and precise fine-tuning of the wetting state. Yet, a microscopic understanding of the mechanism controlling the properties of the superhydrophobic state under electrowetting (EW) conditions and in particular the stability limit of the Cassie state is lacking. Such a detailed understanding will be crucial to reach the holy grail of reversible switching between these states, which has so far been limited to a few special cases involving partial evaporation, violent mechanical shaking, and specific water-in-oil systems.

The Cassie state is associated with very low resistance to droplet motion. To sustain the Cassie state, either reversibility of the Cassie-Wenzel transition should be achieved or the surface must be designed such that the energy barrier for a transition to the Wenzel state is extremely high. Bahadur and Garimella [74] identified contact angle retraction as a necessary condition for the reverse transition from the Wenzel state to the Cassie state. Four EW reversal mechanisms have been demonstrated to date. Krupenkin et al. [75] achieved reversible transition by vaporizing the liquid in immediate contact with pillars by means of a heat pulse through the pillar substrate. Dhindsa et al. [76] showed that reversibility can be achieved through competitive two-liquid EW. Manukyan et al. [77] achieved reversibility by changing only a part of the interface to the Wenzel state, while

other regions of the drop substrate interface remain in the Cassie state. This causes the Wenzel state without EW forces to be highly unstable and hence the interface transitions to the Cassie state. However, the method is not useful when the Wenzel transition happens all across the interface. Recently, Kumari and Garimella [78] proposed the inclusion of an additional electrode to obtain complete Cassie-Wenzel reversal of a droplet between two plates. The other method of maintaining the Cassie state is to completely prevent the Cassie-Wenzel transition through the design of robust surfaces. Some promising robust surfaces include double roughness, non-communicating roughness, and re-entrant cavity surfaces. Analytical and experimental research has corroborated the strong effect of surface morphology on the impact behavior of a water droplet and its ability to bounce off the surface. Jung and Bhushan [79] formulated an expression for the critical velocity of the droplet (based on the capillary pressure and the Bernoulli pressure) beyond which water droplets transition to a Wenzel state on textured surfaces. Varanasi et al. [80] developed a pressure-balance model to arrive at a condition for droplet infiltration into the air gap between the surface structures. Denser textured surfaces are expected to provide greater capillary pressure and superior resistance to Wenzel wetting of impacting droplets. To better understand the effect of these robust surfaces, a thorough understanding of the droplet states and the transition mechanisms under EW actuation is required. Bahadur and Garimella [81] developed an energy minimization framework to predict the apparent contact angle of a droplet in the Cassie and Wenzel states on a structured surface under the action of EW forces. The modified sessile Cassie and Wenzel contact angles are given by:

$$\cos \theta_c^e = (-1 + \phi (1 + \cos \theta_0 + \eta)), \quad (6.3)$$

$$\cos \theta_w^e = r_m (\cos \theta_0 + \eta), \quad (6.4)$$

where  $\phi$  is the area fraction covered by the microstructures,  $r_m$  is the true area of the surface to the apparent area, and the electrowetting number  $\eta$  is defined as:

$$\eta = \frac{\epsilon V^2}{2\sigma d}. \quad (6.5)$$

Here,  $d$  is the dielectric thickness,  $\epsilon$  is the dielectric constant,  $V$  is voltage applied, and  $\sigma$  is coefficient of surface tension of the liquid.

Bahadur and Garimella later conducted experiments to validate the energy minimization-based model, to understand different aspects of the Cassie-Wenzel transition, and to analyze the reasons for the lack of reversibility of the transition. The existence of a critical voltage and the reversibility of the Cassie-Wenzel transition were explained in terms of the presence of an energy barrier. The energy minimization methodology and its application to predicting droplet states on superhydrophobic surfaces are summarized in Bahadur and Garimella [81].

### 6.3 RF Switch

Based on the concept described in previous section, CPW capacitive RF switch was designed. Schematic of one of our test devices is shown on Fig. 6.3. This device was designed as two port transmission line (TL) using superhydrophobic structured surface on the top of the RF signal line to be able to measure stub capacitance change due to tunable wetting. In that situation, RF signal line was used also for electrowetting actuation. Switch design is shown in Fig. 6.3 and Fig. 6.4. Circuit model was simulated on ADS and 3-D model confirmed with HFSS.

As shown in Fig. 6.3, when a surface becomes rough, air can remain trapped inside the texture, so that a droplet sits on a composite surface consisting of solid and air. The liquid only contacts its substrate at the top of the asperities. The curvature shape of the liquid can be modified using electrowetting effect, without the need for mechanical systems. Upon applying a voltage between the electrode on the substrate and the liquid metal drop, an electric field is generated that pulls down the liquid surface. The surface

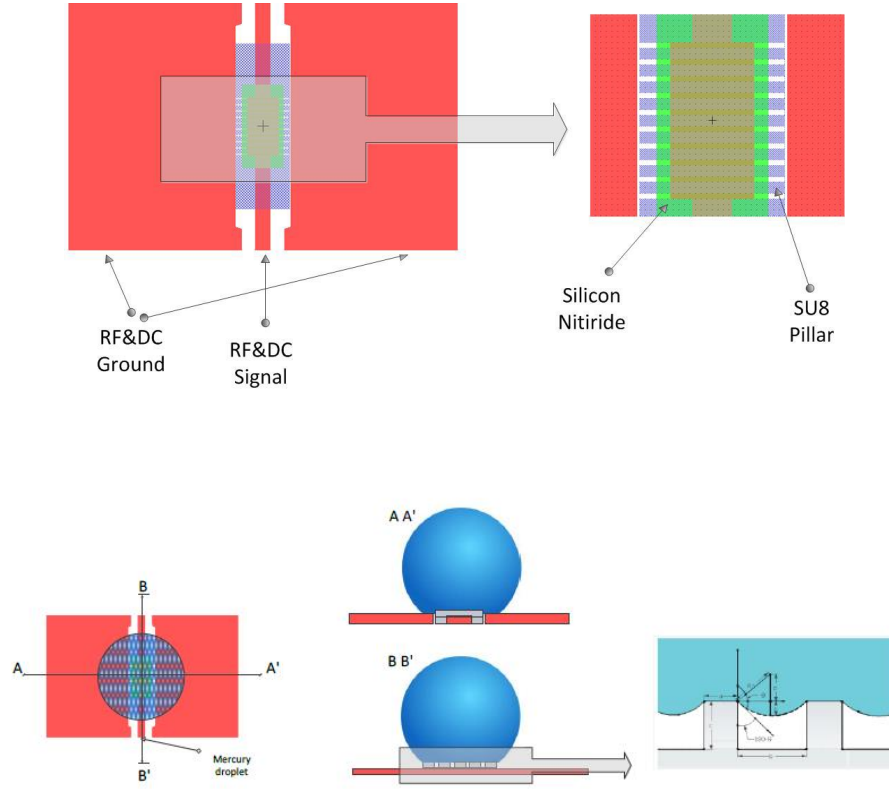


Fig. 6.3: Schematic of capacitive RF switch.

bends until the Laplace pressure caused by the resulting curvature of the interface balances the electric Maxwell stress. This allows the construction of a very simple RF tunable system in which capacitance change easily accomplished with electrical signals instead of mechanical assemblies.

Superhydrophobic surfaces were prepared in cleanroom using microfabrication techniques. Fabrication was consisted of four steps: 1<sup>st</sup> layer, metallization (Cr/Cu/Ni); 2<sup>nd</sup> layer insulator silicon nitride; 3<sup>rd</sup> layer, hydrophobic rectangular pillar (10  $\mu\text{m}$  thick SU8); last step was 100  $\mu\text{m}$  thick SU8 frame as a membrane border. Fabrication of these devices is also inexpensive and easier than MEMS counterparts. Figure 6.5 shows the fabricated device.

RF measurement set-up was built with 150  $\mu\text{m}$  pitch RF probes and bias tees to protect VNA to DC currents. Capacitance change observed by VNA for any given actuation voltage.

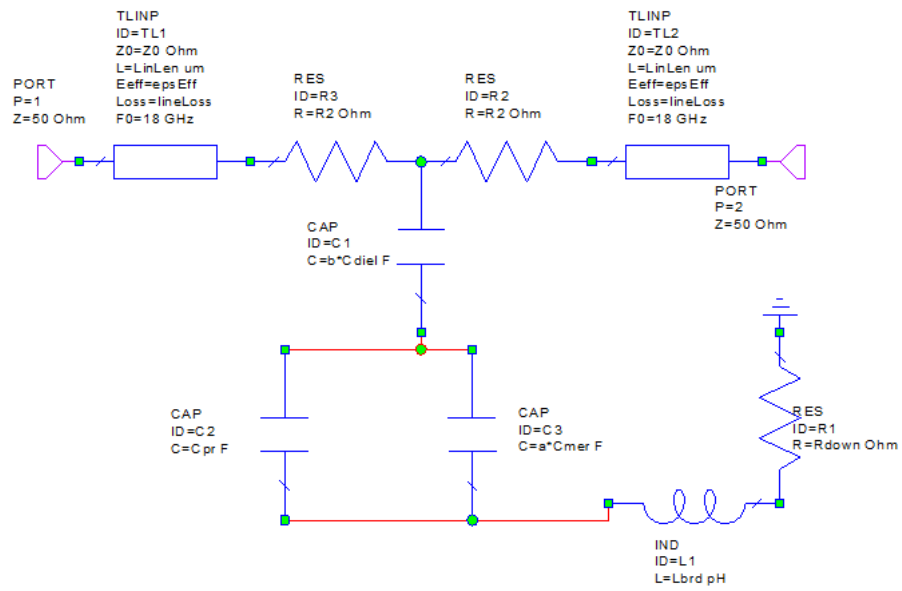


Fig. 6.4: Circuit model of capacitive RF switch.

Measurement results are well correlated with circuit model. Test set-up and measurement results are shown in Fig. 6.6.



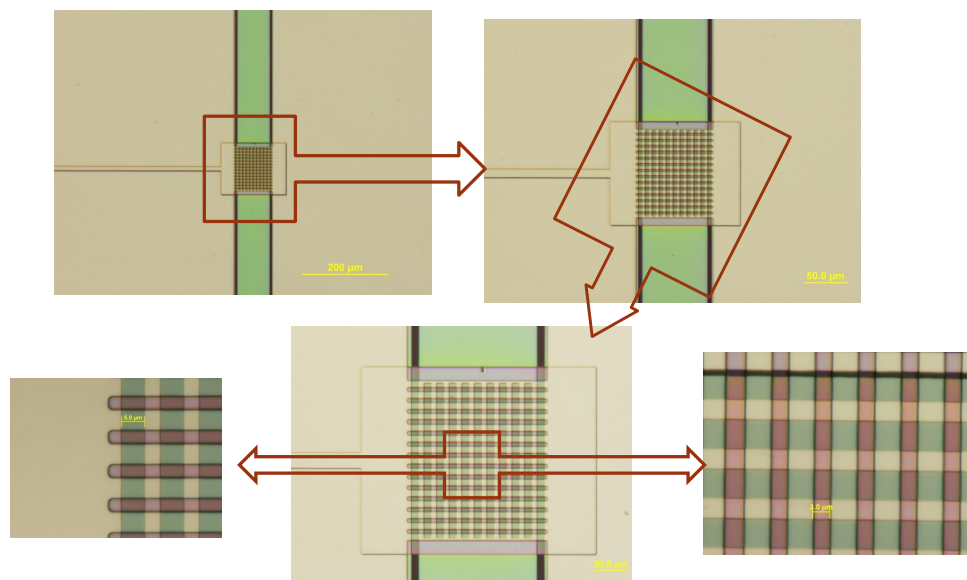
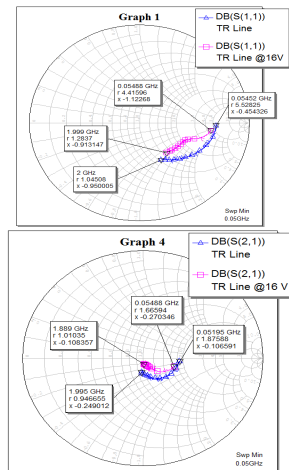


Fig. 6.5: Fabricated RF switch.

### VNA Measurements



### ADS Simulations

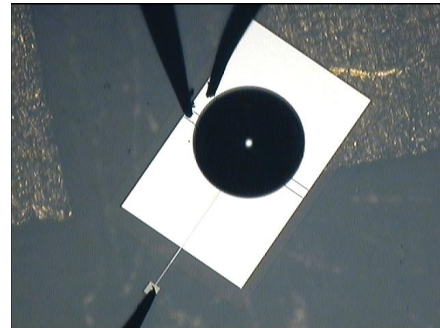
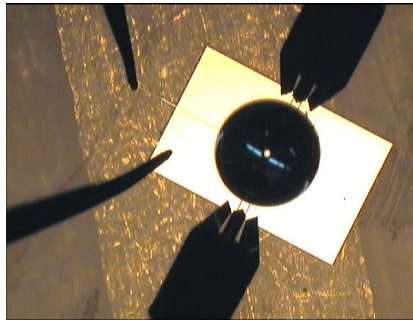
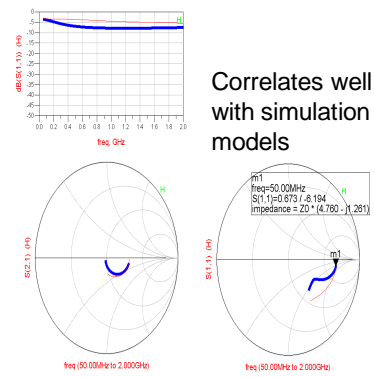


Fig. 6.6: Measurement set-up and results.

## Chapter 7

### Conclusions and Future Work

Reconfigurable antennas consist of two main building blocks: radiation elements and reconfiguration mechanisms. In this work, development of new reconfiguration technology is addressed. Electrowetting on dielectric (EWOD) based digital microfluidics has been demonstrated as a novel reconfiguration technique for antennas. Theoretical and experimental proof is used to show that this technique allows discrete volumes of liquid to be precisely controlled as independent units within microstructures. Three different reconfiguration techniques are presented. The first approach is based on the unique metamaterial transmission line structures, which are leading to antenna miniaturization. Coplanar Waveguide (CPW) metamaterial TLs were designed and used as digital microfluidic platforms, where tunable resonance frequency was demonstrated for RF/microwave applications. The second methodology is based on annular slot antenna integration with a microfluidic chip which consists of EWOD platform having mercury droplet within it. This droplet was spread out by electrostatic actuation thereby resulting in reversible reconfigurable impedance properties. The third methodology was proposing a tunable component using superhydrophobic micro-structured surfaces. These surfaces, along with tunable wetting techniques can be used for transition from the superhydrophobic Cassie state to the normal Wenzel wetting state to build a variable capacitive device (analog varactor, a switched capacitor) or a low-loss switch. The advantage of using first two techniques lies in the fact that they negate the use of bias lines as opposite to RF-MEMS, PIN diodes, lumped elements, and varactors. This has the effect of minimizing perturbations affecting the radiation properties of the antenna structure. The broad impact of this study is a step towards bringing electrowetting technology to the antenna design where fluidic based antennas could be realized with low cost and complexity.

A future study should focus on the nature of the Cassie-Wenzel transition through more detailed measurements. Such a study is expected to enhance the current understanding of the nature and dynamics of the Cassie-Wenzel transition and impact the development of reconfigurable antennas, which have the Cassie-Wenzel transition as a microfluidic operation.

## References

- [1] E. R. Brown, "RF MEMS switches for reconfigurable integrated circuits," *IEEE Transactions on Microwave Theory and Techniques*, vol. 46, no. 11, pp. 1868–1880, 1998.
- [2] J. Papapolymou and J. Bernhard, "Guest editorial for the special issue on multifunction antennas and antenna systems," *IEEE Transactions on Antennas and Propagation*, vol. 54, no. 2, pp. 314–316, 2006.
- [3] J.-C. Langer, J. Zou, C. Liu, and J. Bernhard, "Micromachined reconfigurable out-of-plane microstrip patch antenna using plastic deformation magnetic actuation," *IEEE Microwave and Wireless Components Letters*, vol. 13, no. 3, pp. 120–122, 2003.
- [4] A. Fathy, A. Rosen, H. Owen, F. McGinty, D. McGee, G. Taylor, R. Amantea, P. Swain, S. Perlow, and M. ElSherbiny, "Silicon-based reconfigurable antennas-concepts, analysis, implementation, and feasibility," *IEEE Transactions on Microwave Theory and Techniques*, vol. 51, no. 6, pp. 1650–1661, 2003.
- [5] G. H. Huff and J. T. Bernhard, *Reconfigurable Antennas*. Hoboken, NJ: John Wiley and Sons, Inc., 2007.
- [6] N. Behdad and K. Sarabandi, "Dual band reconfigurable antenna with a very wide tunability range," *IEEE Transactions on Antennas and Propagation*, vol. 54, no. 2, pp. 409–416, 2002.
- [7] D. Anagnostou, G. Zheng, M. Chryssomallis, J. Lyke, G. Ponchak, J. Papapolymou, and C. Christodoulou, "Design, fabrication, and measurements of an rf-mems-based self-similar reconfigurable antenna," *IEEE Transactions on Antennas and Propagation*, vol. 54, no. 2, pp. 422–432, 2006.
- [8] A. Patnaik, D. Anagnostou, C. Christodoulou, and J. Lyke, "Neurocomputational analysis of a multiband reconfigurable planar antenna," *IEEE Transactions on Antennas and Propagation*, vol. 53, no. 11, pp. 3453–3458, 2005.
- [9] A. Patnaik, D. Anagnostou, C. G. Christodoulou, and J. C. Lyke, "A frequency reconfigurable antenna design using neural networks," *Antennas and Propagation Society International Symposium, IEEE*, vol. 2, pp. 409–412, 2005.
- [10] N. Kingsley, D. Anagnostou, M. Tentzeris, and J. Papapolymou, "RF-MEMS sequentially reconfigurable sierpinski antenna on a flexible organic substrate with novel dc-biasing technique," *Journal of Microelectromechanical Systems*, vol. 16, no. 5, pp. 1185–1192, 2007.
- [11] D. Piazza, N. Kirsch, A. Forenza, R. Heath, and K. Dandekar, "Design and evaluation of a reconfigurable antenna array for MIMO systems," *IEEE Transactions on Antennas and Propagation*, vol. 56, no. 3, pp. 869–881, 2008.

- [12] S. DeLuccia, D. Werner, P. Werner, M. Pantoja, and A. Bretones, "A novel frequency agile beam scanning reconfigurable antenna," *Antennas and Propagation Society International Symposium, IEEE*, vol. 2, pp. 1839–1842, 2004.
- [13] F. Ghanem, P. Hall, and J. Kelly, "Two port frequency reconfigurable antenna for cognitive radios," *Electronics Letters*, vol. 45, no. 11, pp. 534–536, 2009.
- [14] A. Mak, C. Rowell, R. Murch, and C.-L. Mak, "Reconfigurable multiband antenna designs for wireless communication devices," *IEEE Transactions on Antennas and Propagation*, vol. 55, no. 7, pp. 1919–1928, 2007.
- [15] A. Cidronali, L. Lucci, G. Pelosi, P. Samori, and S. Selleri, "A reconfigurable printed dipole for quad-band wireless applications," *Antennas and Propagation Society International Symposium, IEEE*, pp. 217–220, 2006.
- [16] M. Ali and P. Wahid, "A reconfigurable yagi array for wireless applications," *Antennas and Propagation Society International Symposium, IEEE*, vol. 1, pp. 466–468, 2002.
- [17] L. Feldner, C. Rodenbeck, C. Christodoulou, and N. Kinzie, "Electrically small frequency-agile PIFA-as-a-package for portable wireless devices," *IEEE Transactions on Antennas and Propagation*, vol. 55, no. 11, pp. 3310–3319, 2007.
- [18] W. Weedon, W. Payne, and G. Rebeiz, "MEMS-switched reconfigurable antennas," *Antennas and Propagation Society International Symposium, IEEE*, vol. 3, pp. 654–657, 2001.
- [19] S. Xiao, B.-Z. Wang, X.-S. Yang, and G. Wang, "Reconfigurable microstrip antenna design based on genetic algorithm," *Antennas and Propagation Society International Symposium, IEEE*, vol. 1, pp. 407–410, 2003.
- [20] V. Zachou, C. Christodoulou, M. Chryssomallis, D. Anagnostou, and S. Barbin, "Planar monopole antenna with attached sleeves," *IEEE Antennas and Wireless Propagation Letters*, vol. 5, no. 1, pp. 286–289, 2006.
- [21] J. Zendejas, J. Gianvittorio, Y. Rahmat-Samii, and J. Judy, "Magnetic MEMS reconfigurable frequency-selective surfaces," *Journal of Microelectromechanical Systems*, vol. 15, no. 3, pp. 613–623, 2006.
- [22] J. Costantine and C. Christodoulou, "A new reconfigurable antenna based on a rotating feed," *Antennas and Propagation Society International Symposium, IEEE*, pp. 1–4, 2008.
- [23] B. Poussot, J.-M. Laheurte, L. Cirio, O. Picon, D. Delcroix, and L. Dussopt, "Diversity measurements of a reconfigurable antenna with switched polarizations and patterns," *IEEE Transactions on Antennas and Propagation*, vol. 56, no. 1, pp. 31–38, 2008.
- [24] T. Roach, G. Huff, and J. Bernhard, "Enabling high performance wireless communication systems using reconfigurable antennas," *Military Communications Conference, MILCOM, IEEE*, pp. 1–6, 2006.

- [25] G. Kang, Z. Du, and K. Gong, "Novel reconfigurable antenna array with pattern diversity," *Asia-Pacific Microwave Conference Proceedings (APMC)*, pp. 1306–1309, 2011.
- [26] B. A. Cetiner, E. Akay, E. Sengul, and E. Ayanoglu, "A MIMO system with multifunctional reconfigurable antennas," *IEEE Antennas and Wireless Propagation Letters*, vol. 5, no. 1, pp. 463–466, 2006.
- [27] H. Aissat, L. Cirio, M. Grzeskowiak, J.-M. Laheurte, and O. Picon, "Reconfigurable circularly polarized antenna for short-range communication systems," *IEEE Transactions on Microwave Theory and Techniques*, vol. 54, no. 6, pp. 2856–2863, 2006.
- [28] M. T. Oswald, S. C. Hagness, B. Van Veen, and Z. Popovic, "Reconfigurable single-feed antennas for diversity wireless communications," *Antennas and Propagation Society International Symposium, IEEE*, vol. 1, pp. 469–472, 2002.
- [29] C. W. Jung, M.-J. Lee, G. P. Li, and F. De Flaviis, "Reconfigurable scan-beam single-arm spiral antenna integrated with rf-mems switches," *IEEE Transactions on Antennas and Propagation*, vol. 54, no. 2, pp. 455–463, 2006.
- [30] F. Yang and Y. Rahmat-Samii, "Patch antenna with switchable slots (PASS): reconfigurable design for wireless communications," *Antennas and Propagation Society International Symposium, IEEE*, vol. 1, pp. 462–465, 2002.
- [31] B. A. Cetiner, H. Jafarkhani, J.-Y. Qian, H. J. Yoo, A. Grau, and F. De Flaviis, "Multifunctional reconfigurable MEMS integrated antennas for adaptive MIMO systems," *IEEE Communications Magazine*, vol. 42, no. 12, pp. 62–70, 2004.
- [32] H. De Los Santos, *Introduction to Microelectromechanical Microwave Systems*, ser. Artech House microelectromechanical systems series. Norwood, MA: Artech House, 2004.
- [33] C. Luxey, L. Dussopt, J.-L. Le Sonn, and J.-M. Laheurte, "Dual-frequency operation of CPW-fed antenna controlled by pin diodes," *Electronics Letters*, vol. 36, no. 1, pp. 2–3, 2000.
- [34] S. Kawasaki and T. Itoh, "A slot antenna with electronically tunable length," *Antennas and Propagation Society International Symposium, IEEE*, pp. 130–133 vol. 1, 1999.
- [35] J. Zammit and A. Muscat, "A small tunable antenna using multiple shorting posts and varactor diodes," *3rd International Symposium on Communications, Control and Signal Processing, ISCCSP*, pp. 83–86, 2008.
- [36] S. Gevorgian and E. Kollberg, "Do we really need ferroelectrics in paraelectric phase only in electrically controlled microwave devices?" *IEEE Transactions on Microwave Theory and Techniques*, vol. 49, no. 11, pp. 2117–2124, 2001.
- [37] P. Rainville and F. Harackiewicz, "Magnetic tuning of a microstrip patch antenna fabricated on a ferrite film," *IEEE Microwave and Guided Wave Letters*, vol. 2, no. 12, pp. 483–485, Dec. 1992.

- [38] D. Pozar and V. Sanchez, "Magnetic tuning of a microstrip antenna on a ferrite substrate," *Electronics Letters*, vol. 24, no. 12, pp. 729–731, June 1988.
- [39] R. Mishra, S. Pattnaik, and N. Das, "Tuning of microstrip antenna on ferrite substrate," *IEEE Transactions on Antennas and Propagation*, vol. 41, no. 2, pp. 230–233, Feb. 1993.
- [40] M. Kohl, *Shape Memory Microactuators*, ser. Microtechnology and MEMS. Heidelberg, Germany: Springer, 2004.
- [41] D. Sievenpiper, J. Schaffner, R. Loo, G. Tangonan, S. Ontiveros, and R. Harold, "A tunable impedance surface performing as a reconfigurable beam steering reflector," *IEEE Transactions on Antennas and Propagation*, vol. 50, no. 3, pp. 384–390, Mar. 2002.
- [42] D. Sievenpiper, J. Schaffner, H. Song, R. Loo, and G. Tangonan, "Two-dimensional beam steering using an electrically tunable impedance surface," *IEEE Transactions on Antennas and Propagation*, vol. 51, no. 10, pp. 2713–2722, Oct. 2003.
- [43] D. Sievenpiper, J. Schaffner, J. Lee, and S. Livingston, "A steerable leaky-wave antenna using a tunable impedance ground plane," *IEEE Antennas and Wireless Propagation Letters*, vol. 1, no. 1, pp. 179–182, 2002.
- [44] D. Sievenpiper and J. Schaffner, "Beam steering microwave reflector based on electrically tunable impedance surface," *Electronics Letters*, vol. 38, no. 21, pp. 1237–1238, Oct. 2002.
- [45] D. Sievenpiper, "Forward and backward leaky wave radiation with large effective aperture from an electronically tunable textured surface," *IEEE Transactions on Antennas and Propagation*, vol. 53, no. 1, pp. 236–247, Jan. 2005.
- [46] S. Cheng, A. Rydberg, K. Hjort, and Z. Wu, "Liquid metal stretchable unbalanced loop antenna," *Applied Physics Letters*, vol. 94, no. 14, p. 144103, 2009.
- [47] J.-H. So, J. Thelen, A. Qusba, G. J. Hayes, G. Lazzi, and M. D. Dickey, "Reversibly deformable and mechanically tunable fluidic antennas," *Advanced Functional Materials*, vol. 19, no. 22, 2009.
- [48] G. Huff, D. Rolando, P. Walters, and J. McDonald, "A frequency reconfigurable dielectric resonator antenna using colloidal dispersions," *Antennas and Wireless Propagation Letters, IEEE*, vol. 9, pp. 288–290, 2010.
- [49] J. Berthier, *Micro-Drops and Digital Microfluidics*, ser. Micro and Nano Technologies. Norwich, NY: Elsevier Science, 2012.
- [50] F. Mugele and J.-C. Baret, "Electrowetting: from basics to applications," *Journal of Physics: Condensed Matter*, vol. 17, no. 28, p. R705, 2005.
- [51] T. B. Jones, J. D. Fowler, Y. S. Chang, and C.-J. Kim, "Frequency-based relationship of electrowetting and dielectrophoretic liquid microactuation," *Langmuir*, vol. 19, no. 18, pp. 7646–7651, 2003.



- [52] T. B. Jones, "On the relationship of dielectrophoresis and electrowetting," *Langmuir*, vol. 18, no. 11, pp. 4437–4443, 2002.
- [53] J. Schwinger, L. Deraad, and K. Milton, *Classical Electrodynamics*, ser. Advanced book program. Boulder, CO: Westview Press, 1998.
- [54] K. H. Kang, "How electrostatic fields change contact angle in electrowetting," *Langmuir*, vol. 18, no. 26, pp. 10 318–10 322, 2002.
- [55] F. Mugele and J. Buehrle, "Equilibrium drop surface profiles in electric fields," *Journal of Physics: Condensed Matter*, vol. 19, no. 37, p. 375112, 2007.
- [56] J. Buehrle, S. Herminghaus, and F. Mugele, "Interface profiles near three-phase contact lines in electric fields," *Physical Review Letters*, vol. 91, no. 8, p. 086101, 2003.
- [57] M. P. and C. M. Soukoulis, "Transmission studies of left-handed materials," *Physical Review B*, vol. 65, p. 033401, Dec. 2001.
- [58] R. Ziolkowski, "Pulsed and CW Gaussian beam interactions with double negative metamaterial slabs," *Optics Express*, vol. 11, no. 7, pp. 662–681, Apr. 2003.
- [59] C. Caloz, C.-C. Chang, and T. Itoh, "Full-wave verification of the fundamental properties of left-handed materials in waveguide configurations," *Journal of Applied Physics*, vol. 90, no. 11, pp. 5483–5486, 2001.
- [60] P. M. So and W. J. R. Hoefer, "Time domain TLM modelling of metamaterials with negative refractive index," *MTT-S International Microwave Symposium Digest, IEEE*, vol. 3, pp. 1779–1782, 2004.
- [61] J. A. Kong, B.-I. Wu, and Y. Zhang, "A unique lateral displacement of a gaussian beam transmitted through a slab with negative permittivity and permeability," *Microwave and Optical Technology Letters*, vol. 33, no. 2, pp. 136–139, 2002.
- [62] A. Lai, T. Itoh, and C. Caloz, "Composite right/left-handed transmission line metamaterials," *IEEE Microwave Magazine*, vol. 5, no. 3, pp. 34–50, 2004.
- [63] B. Zhao, R. Shi, and A. Ferendeci, "Zeroth order resonator antennas using composite right/left-handed microstrip transmission lines," *Aerospace and Electronics Conference, NAECON, IEEE National*, pp. 154–158, 2008.
- [64] C. P. Lai, S. C. Chiu, H. J. Li, and S. Y. Chen, "Zeroth order resonator antennas using inductor-loaded and capacitor loaded CPWs," *IEEE Transactions on Antennas and Propagation*, vol. 59, no. 9, pp. 3448–3453, 2011.
- [65] S. G. Mao, S. L. Chen, and C. W. Huang, "Effective electromagnetic parameters of novel distributed left handed microstrip lines," *IEEE Transactions on Microwave Theory and Techniques*, vol. 53, no. 4, pp. 1515–1521, 2005.
- [66] U. C. Yi and C. J. Kim, "Characterization of electrowetting actuation on addressable single side coplanar electrodes," *Journal of Micromechanics and Microengineering*, vol. 16, no. 10, p. 2053, 2006.

- [67] P. Sen and C. J. Kim, “A fast liquid metal droplet microswitch using ewod driven contact line sliding,” *Journal of Microelectromechanical Systems*, vol. 18, no. 1, pp. 174–185, 2009.
- [68] Z. Wan, H. Zeng, and A. Feinerman, “Area tunable micromirror based on electrowetting actuation of liquid metal droplets,” *Applied Physics Letters*, vol. 89, no. 20, p. 201107, 2006.
- [69] H. Zeng, Z. Wan, and A. Feinerman, “Tilting micromirror with a liquid metal pivot,” *Journal of Microelectromechanical Systems*, vol. 15, no. 6, pp. 1568–1575, 2006.
- [70] M. G. Pollack, A. D. Shenderov, and R. B. Fair, “Electrowetting based actuation of droplets for integrated microfluidics,” *Lab Chip*, vol. 2, pp. 96–101, 2002.
- [71] C. Cooney, C. Y. Chen, M. Emerling, A. Nadim, and J. Sterling, “Electrowetting droplet microfluidics on a single planar surface,” *Microfluidics and Nanofluidics*, vol. 2, pp. 435–446, 2006.
- [72] S. H. Ko, H. Lee, and K. H. Kang, “Hydrodynamic flows in electrowetting,” *Langmuir*, vol. 24, no. 3, pp. 1094–1101, 2008.
- [73] D. Quéré, “Non-sticking drops,” *Reports on Progress in Physics*, vol. 68, no. 11, p. 2495, 2005.
- [74] V. Bahadur and S. Garimella, “An energy-based model for electrowetting-induced droplet actuation,” *Journal of Micromechanics and Microengineering*, vol. 16, no. 8, p. 1494, 2006.
- [75] T. N. Krupenkin, J. A. Taylor, T. M. Schneider, and S. Yang, “From rolling ball to complete wetting: the dynamic tuning of liquids on nanostructured surfaces,” *Langmuir*, vol. 20, no. 10, pp. 3824–3827, 2004.
- [76] M. S. Dhindsa, N. R. Smith, J. Heikenfeld, P. D. Rack, J. D. Fowlkes, M. J. Doktycz, A. V. Melechko, and M. L. Simpson, “Reversible electrowetting of vertically aligned superhydrophobic carbon nanofibers,” *Langmuir*, vol. 22, no. 21, pp. 9030–9034, 2006.
- [77] G. Manukyan, J. Oh, D. Van Den Ende, R. Lammertink, and F. Mugele, “Electrical switching of wetting states on superhydrophobic surfaces: A route towards reversible cassie-to-wenzel transitions,” *Physical Review Letters*, vol. 106, no. 1, p. 014501, 2011.
- [78] N. Kumari and S. V. Garimella, “Electrowetting-induced dewetting transitions on superhydrophobic surfaces,” *Langmuir*, vol. 27, no. 17, pp. 10 342–10 346, 2011.
- [79] Y. C. Jung and B. Bhushan, “Dynamic effects induced transition of droplets on biomimetic superhydrophobic surfaces,” *Langmuir*, vol. 25, no. 16, pp. 9208–9218, 2009.
- [80] K. K. Varanasi, T. Deng, J. D. Smith, M. Hsu, and N. Bhate, “Frost formation and ice adhesion on superhydrophobic surfaces,” *Applied Physics Letters*, vol. 97, no. 23, pp. 234 102–1–234 102–3, 2010.

- [81] V. Bahadur and S. Garimella, “Energy minimization-based analysis of electrowetting for microelectronics cooling applications,” *Microelectronics Journal*, vol. 39, no. 7, pp. 957–965, 2008.

## Appendix

## Sessile Droplet Morphology

A droplet at micro-scale has the form of a spherical shape in order to minimize its surface energy if only surface tension is considered at the droplet-solid interface. Figure A.1 shows the cross section view of a liquid droplet dispensed on a hydrophobic surface. The volume  $V$  of such a droplet is a function of four parameters,  $\theta$ ,  $a$ ,  $R$ ,  $h$ , where  $\theta$  is the contact angle,  $a$  is the contact radius (i.e., the radius of the circular base),  $R$  is the curvature radius (i.e., the sphere radius), and  $h$  is the height of the droplet. The height of the droplet,  $h$ , and contact radius,  $a$ , are expressed:

$$h = R + R \cos(\pi - \theta) = R(1 - \cos \theta), \quad (\text{A.1})$$

$$h = R \times \cos\left(\theta - \frac{\pi}{2}\right) = R \times \sin(\pi - \theta) = R \times \sin \theta. \quad (\text{A.2})$$

The volume of a droplet (Fig. A.2) can be obtained the integration of Eq. (A.3).

$$V = \int_{-(h-R)}^R \pi r^2 dz = \frac{\pi h^2}{3} (3R - h) \quad (\text{A.3})$$

Combining Eqs. (A.1), (A.2), and (A.3), the height of a droplet can be calculated by:

$$h = R(1 - \cos \theta) = \left( \sqrt[3]{\frac{3V}{\pi(2 - 3\cos \theta + \cos^3 \theta)}} \right) (1 - \cos \theta). \quad (\text{A.4})$$

For the same volume of a droplet, its height can be determined by the contact angle, which can be measured directly from the goniometer.

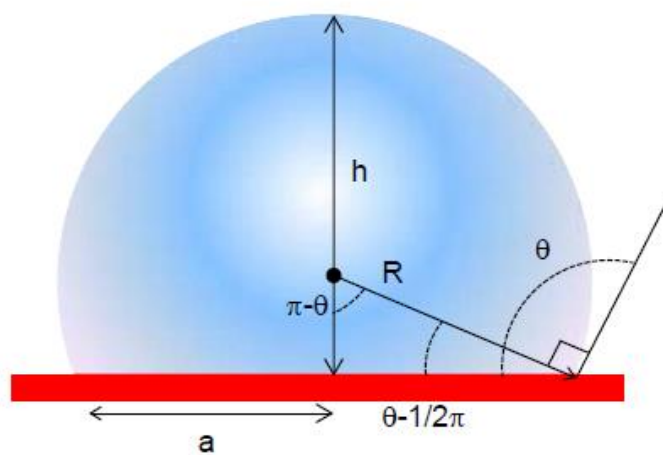


Fig. A.1: Cross section view of a micro-drop dispensed on a hydrophobic surface.

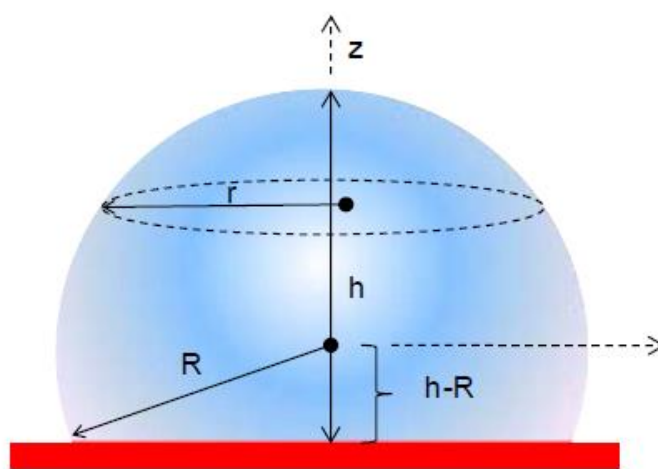


Fig. A.2: Schematic of a droplet for volume integration.

## Vita

### Yasin Damgaci

#### Patents

- Reconfigurable Antennas Utilizing Liquid Metal Elements Inventors: Bedri A. Cetiner, Yasin Damgaci, Luis Jofre, Daniel Rodrigo- PCTUS/2012/068386.
- Tunable microfluidic RF/Microwave/millimeter-wave systems based on wetting transition on superhydrophobic surfaces - Inventors: Yasin Damgaci, Bedri A. Cetiner -Utah State University Intellectual Property Office ID: D12028.

#### Journal Articles

- Frequency Reconfigurable Antenna based on Digital Microfluidics, Yasin Damgaci, Bedri A. Cetiner, *Lab on a Chip, Accepted for publication.*
- Tunable Zeroth Order Resonance in Metamaterial Transmission Lines based on Electrowetting on Dielectric (EWOD), Yasin Damgaci, Bedri A. Cetiner, *IEEE Microwave and Wireless Components Letters, Accepted for publication.*
- Nanoelectromechanical Switches for Reconfigurable Antenna Applications, B. A. Cetiner, B. S. Yildirim, N. Biyikli, and Y. Damgaci *Microwave and Optical Technology Letters*, vol. 1, pp. 64-69, 2010.
- A low-voltage small-size double-arm MEMS actuator, B. A. Cetiner, N. Biyikli, Y. Damgaci, and B. A. Cetiner *IEE Electronics Letters*, vol. 45, 2009

## Conference Papers

- Actuation of Liquid Metal Droplets Using Electrowetting-on-Dielectric (EWOD) for Reconfigurable Antenna Applications, Engin Cagatay, Y. Damgaci, Bedri A. Cetiner and Necmi Biyikli in *Materials Research Society Fall Meeting*, 2011
- Actuation of Liquid Metal Droplets Using Electrowetting-on-dielectric (EWOD), Engin Cagatay, Y. Damgaci, Bedri A. Cetiner and Necmi Biyikli in *(NanoTR VII) 7th Nanoscience and Nanotechnology Conference*, 2011.
- Reconfigurable, tri-band RF MEMS PIFA Antenna, Unlu Mehmet; Y, Damgaci; Mopidevi, Hema S.; Kaynar, Oguz; Cetiner, Bedri A. Cetiner, *IEEE AP-S*, 2011.
- Genetic Reconfigurability of a Multi-Size Pixelled Antena, Rodrigo, D.; Unlu, M.; Y, Damgaci.; Cetiner, B.A.; Romeu, J.; Jofre, L., in *IEEE Conference on Wireless Information Technology and Systems*, 2010.
- MEMS-Reconfigurable Antenna based on a Multi-Size Pixelled Geometry, D. Rodrigo, Y. Damgaci, N. Biyikli, Bedri A. Cetiner , J. Romeu and L. Jofre, *Proceedings of the Fourth European Conference on Antennas and Propagation (EuCAP)*, 2010
- MEMS Integrated Reconfigurable Antenna for Cognitive Public Safety Radios, A. Khoshniat, H. Mopidevi, Y. Damgaci, D. Rodrigo, L. Jofre and B. A. Cetiner, *Proceedings of the Fourth European Conference on Antennas and Propagation (EuCAP)*, 2010
- Polarization Reconfigurable MEMS-CPW Antenna for mm-wave Applications, J. Balcells, Y. Damgaci, Bedri A. Cetiner, J. Romeu, L. Jofre, in *Proceedings of the Fourth European Conference on Antennas and Propagation (EuCAP)*, 2010.
- Full-wave analysis of 60 GHz reconfigurable antenna for WPAN Applications, X. Yuan, Y. Damgaci, and B. A. Cetiner, in *Progress in Electromagnetic Research Symposium (PIERS)*, 2010.



- Genetic Impedance and Radiation Reconfigurability of a NEMS Bi-Clustered Pixelled Antenna, D. Rodrigo, Y. Damgaci, N. Biyikli, B.A.Cetiner, L. Jofre , in *MEMSWAVE*, 2009.
- Genetic impedance and radiation reconfigurability of a NEMS bi-clustered pixelled antenna, Rodrigo, D.; Y, Damgaci.; Biyikli, N.; Cetiner, B.A.; Romeu, J.; Jofre, L., in *The 10th International Symposium on RF MEMS and RF Microsystems*, 2009.
- RF-NEMS Integrated Frequency Reconfigurable Antenna for Waveform Diversity Schemes, Y. Damgaci, X. Yuan, N. Biyikli, and B. A. Cetiner, in *URSI*, 2009.
- RF-N/MEMS Integrated Reconfigurable Antenna for Public Safety Applications, X. Yuan, Y. Damgaci, H. Mopidevi, and B. A. Cetiner , in *IEEE AP-S*, 2009.